UNIVERSITY
OF TWENTE.

Singularities With Surfactants

Jnandeep Talukdar

Energy and Flow
Department of Mechanical Engineering
Master in Mechanical Engineering

Enschede, June 2025

This page intentionally left blank.

Singularities With Surfactants

Jnandeep Talukdar

Supervisor: Prof. Detlef Lohse
Chair, Physics of Fluids (University of Twente)

Co-supervisor: Dr. Vatsal Sanjay
Postdoctoral Researcher, University of Twente

Energy and Flow
Department of Mechanical Engineering
Master in Mechanical Engineering

Master's Thesis

Enschede, June 2025

This page intentionally left blank.

DECLARATION OF AUTHORSHIP

Has undersigned, hereby it his declared that this work entitled “Singularities With Surfactants” is the original work and that it has not previously in its entirety or in part been submitted at any university or higher education institution for the award of any degree, diploma, or other qualifications. It is also hereby declared that to the best of the knowledge, this work contains no material previously published or written by another person, except where due reference, acknowledgement, and citation is made.

Enschede, June 2025

Jnandeep Talukdar

This page intentionally left blank.

Abstract

Drop coalescence originates from a finite-time hydrodynamic singularity–the moment when two interfaces merge and a liquid bridge forms from zero radius. This topological transition exemplifies how singular events in fluid mechanics exhibit self-similar dynamics and universal scaling laws, providing fundamental insights into nonlinear phenomena. While these singularities have been extensively studied in pure fluids, most practical liquids, such as those used in inkjet printing, pharmaceutical emulsions, food products, and oil recovery, contain surfactants that fundamentally alter the singular behavior by coupling surface chemistry to flow. Here we investigate how insoluble surfactants modify coalescence singularities through high-fidelity numerical simulations and theoretical modeling, considering a surfactant-laden drop merging with a clean drop.

The dynamics are governed by three dimensionless parameters: the surfactant strength number β quantifying the relative change in surface tension, the surface Péclet number Pe representing advection-to-diffusion ratio, and the initial contact angle θ. In the diffusion-dominated regime ($Pe \ll 1$), the singularity retains its self-similar character with neck height evolving as $h_0 = 0.272(1 - \beta\Gamma_0/2)\theta^4 t$–preserving the linear scaling but modified by surfactant-induced surface tension reduction. Remarkably, Marangoni stresses break the symmetry of the singularity, driving horizontal neck motion as $x_0 \propto t^{3/2}$, a phenomenon absent in pure systems.

The advection-dominated regime ($Pe \gg 1$) reveals how surfactants can fundamentally alter the singular dynamics. Above a critical strength β_c (≈ 0.15 for $\theta = 20^\circ$), the singularity arrests into a stable non-coalescent state, while below this threshold, interfacial vorticity generation enables escape. At $Pe \to \infty$, new singularities emerge: kinematic shocks with discontinuous velocity and pressure fields, which we interpret through a complex-variable formulation yielding Burgers-like equations. These findings demonstrate how surfactants not only modify existing hydrodynamic singularities but can generate entirely new singular phenomena, with implications spanning from fundamental nonlinear dynamics to industrial applications.

Keywords: droplet, coalescence, lubrication, surfactants, Marangoni flows

CONTENTS

Contents vii

List of Figures xi

List of Tables xv

1 Introduction 1
- 1.1 Singularity and Self-Similarity 2
- 1.2 Drop Coalescence 3
- 1.3 Surfactants 5
- 1.4 Drop Coalescence in Presence of Surfactants 6
- 1.5 Guide Through the Thesis 7

2 Methodology 9
- 2.1 Problem Formulation 9
- 2.2 Governing Equations 10
  - 2.2.1 Non-Dimensional Parameters 12
- 2.3 Numerical Scheme 13

3 Drop coalescence: Low Pe limit 14
- 3.1 Evolution of the Drop Height 14
  - 3.1.1 Early-Time Behavior 15
  - 3.1.2 Diffusive Time Scale and the Temporal Boundary Layer 16
- 3.2 Theory 17
  - 3.2.1 Surfactant Profile 17
  - 3.2.2 Height Profile 18
  - 3.2.3 Horizontal Movement 21
- 3.3 Summary 24

4 Intermezzo: Maximum Horizontal Movement 25
- 4.1 Scaling Laws in the Low Pe Regime 26
- 4.2 Non-Monotonic Behaviour 27
- 4.3 Summary 28

5 Drop Non-Coalescence: High Pe Limit **29**
5.1 Escape from Non-Coalescence 29
5.1.1 Vorticity Generation at the Free Surface 31
5.2 Shock Solutions at High Pe 34
5.3 $1/Pe = 0$ Limit 34
5.3.1 Similarity Transform 36
5.3.2 Traveling Wave Solutions 37
5.4 Summary 38

6 Conclusion & Outlook **40**
6.1 Broader Implications 41
6.2 Limitations and Open Questions 41
6.3 Future Directions 42
6.4 Closing Perspective 43

7 Code Listings **44**

Appendices

A Derivation of lubrication equations for thin liquid films **58**

B Surfactant advection diffusion equation at the interface **62**

This page intentionally left blank.

List of Figures

1.1 Various examples of free-surface flows in nature 2
1.2 Early experimental setup of J.J. Thomson to study coalescence of drops onto a bath, and observed vortex formation 3
1.3 Visualization of series of events in inkjet printing, and different geometries for coalescence 4
1.4 Side-by-side visualization of coalescence and non-coalescence of drops 7

2.1 Physical setup of the study: surfactant-mediated coalescence between two viscous drops 9
2.2 Lubrication model for thin film dynamics with interfacial surfactant transport 10

3.1 Bridge growth and flow evolution in the low-Pe regime: Laplace pressure-driven 14
3.2 Early-time Marangoni-driven and pressure-driven flow dynamics during drop coalescence 15
3.3 Temporal boundary layer and diffusive flattening of surfactant concentration profiles 16
3.4 Neck height h_0 grows linearly in time and depends strongly on θ, but weakly on β or Pe 19
3.5 Data collapse confirms $h_0 = \left(1 - \frac{\beta\Gamma_0}{2}\right)\theta^4 t$ scaling for low Pe 20
3.6 Neck position x_0 shows $t^{3/2}$ scaling from Marangoni flow, with collapse onto theory after compensation 22

4.1 Marangoni forces dominate at $t = 0^+$; geometry-induced Laplace pressure drives flow at $t = t^*$ 25
4.2 Maximum neck displacement scales as $x_f \propto \beta Pe$ in the low-Pe regime . 26
4.3 At high Pe, only $\beta > \beta_c$ leads to significant neck displacement despite similar flow fields 28

5.1 For $\beta = 0.5$, $u_s > 0$ everywhere; monotonic Γ and single-peaked Marangoni stress drive neck rightward 30

5.2 For $\beta = 0.1$, bidirectional surfactant transport creates a non-monotonic profile and opposing Marangoni peaks 32
5.3 Strong vorticity generation for $\beta = 0.1$ promotes coalescence; minimal vorticity for $\beta = 0.5$ 33
5.4 Kinematic shock forms and propagates in the high-Pe regime, marking the edge of the surfactant-laden region. 34
5.5 At $1/Pe = 0$, surfactant fronts persist, neck height is static, and x_0 grows linearly 35

LIST OF TABLES

1.1 Overview of various adsorption isotherms with corresponding source terms and surface pressures 6

2.1 List of dimensionless parameters involved in the problem 13

This page intentionally left blank.

1

INTRODUCTION

Drop coalescence represents one of the most fundamental topological transitions in fluid mechanics, where two separate liquid volumes merge through the formation of a connecting bridge. This singular event – the moment when interfaces touch and a liquid bridge forms from zero radius – exemplifies how finite-time hydrodynamic singularities govern the dynamics of free surface flows. This ubiquitous phenomenon occurs across length scales from nanometers to meters, playing crucial roles in processes ranging from rain formation in clouds to the stability of pharmaceutical emulsions. While pure fluid coalescence reveals universal scaling laws and self-similar behavior near the singularity, most practical liquids contain surface-active molecules that fundamentally alter these singular dynamics by coupling surface chemistry to hydrodynamics through Marangoni stresses.

Free surface flows are a distinct category in fluid mechanics, where the interface separating different phases or fluids evolves dynamically and is not known beforehand (for example, see Figure 1.1a-b where impacting drop creates a splash as it impacts a liquid bath), unlike confined flows such as those in pipes. The coalescence of liquid drops is part of a broader class of free surface flows as the interface separating different phases evolves dynamically and is not known apriori, in contrast to confined flows such as those in pipes. The wind-driven waves formed at the surface of an ocean, the flow of water falling out of a faucet, and even the gravity-driven flow of rivers are examples of free surface flows. These flows are important to numerous industrial processes, including inkjet printing (Lohse, 2022; Basaran et al., 2013), sprays (Lefebvre, 1988), and medical diagnostics (Daly et al., 2015). They also play a role in chemical separations (Ptasinski and Kerkhof, 1992), coating applications (Kistler and Scriven, 1984; Snoeijer and Andreotti, 2013), and electrosprays (Jaworek and Sobczyk, 2008). Beyond industrial applications, free surface flows are fundamental to natural phenomena such as mist formation in waterfalls, raindrop fragmentation in thunderclouds (Villermaux and Bossa, 2009), tidal formation, and water dripping from a faucet (Eggers, 1997; Champougny et al., 2024). The deformation of the interface in these flows must be determined as part of solving the problem, adding to their complexity and significance.

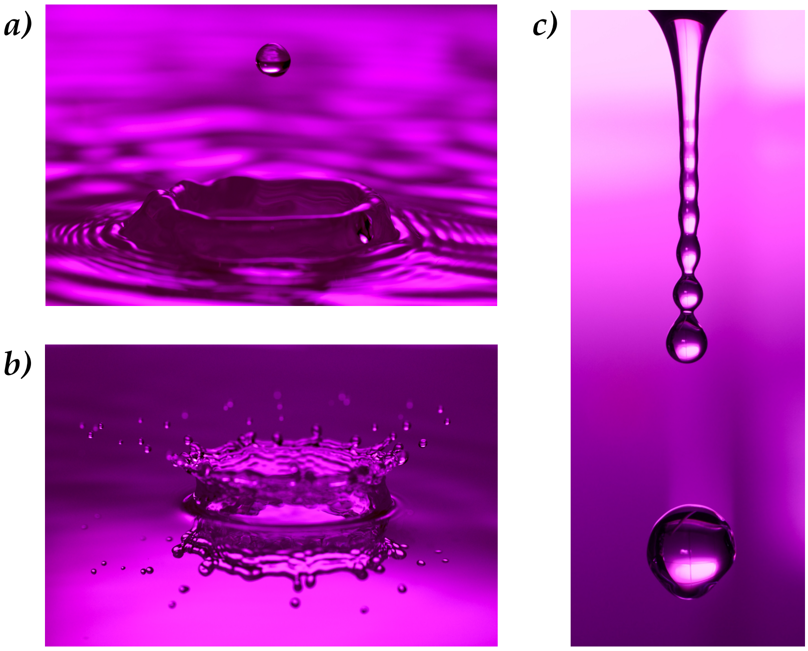

Figure 1.1: ***a*)** *A drop deposited on a bath, leads to a cascade of partial coalescence* ***b*)** *Drop impacting a wetted surface creates a characterisitic crown (See PoF logo)* ***c*)** *A stream of liquid breaks into drops due to Rayleigh-Plateau breakup ©Niklas Morberg*

Some of the earliest investigations on free surface flows were conducted by Leonardo da Vinci in the sixteenth century (Da Vinci, 1508); in his Codex Leicester (Da Vinci, 1980) he studied the behavior of liquid jets and how they break. This and the works of others that followed (Mariotte, 1686) over the next two centuries display the early proto-scientific development of the field of free surface flows. The study of free surface flows dates back to the foundational work of Savart, 1833, Plateau, 1857, and Rayleigh (1878, 1879, 1892), who investigated the behavior of drops, jets, and liquid sheets under perturbations. Rayleigh (1879) demonstrated that fluid jets subjected to long-wavelength disturbances tend to break up into multiple droplets to minimize surface energy. Building on this, modern research has focused on drop formation due to filament and jet breakup, drop coalescence, and film rupture, employing theoretical models, numerical simulations, and experiments (Eggers, 1997; Eggers et al., 1999; McKinley, 2005; Craster and Matar, 2009; Eggers et al., 2024; Dixit et al., 2025). These studies have significantly contributed to both scientific understanding and technological advancements in applications such as inkjet printing, sprays, and coatings.

1.1 Singularity and Self-Similarity

The formation of a liquid bridge during coalescence exemplifies a finite-time singularity, where a characteristic length scale—the bridge radius—emerges from zero in finite time, causing a breakdown in the regularity of the governing Navier–Stokes free surface equations (Tao, 2019). A similar singularity arises in the reverse process of

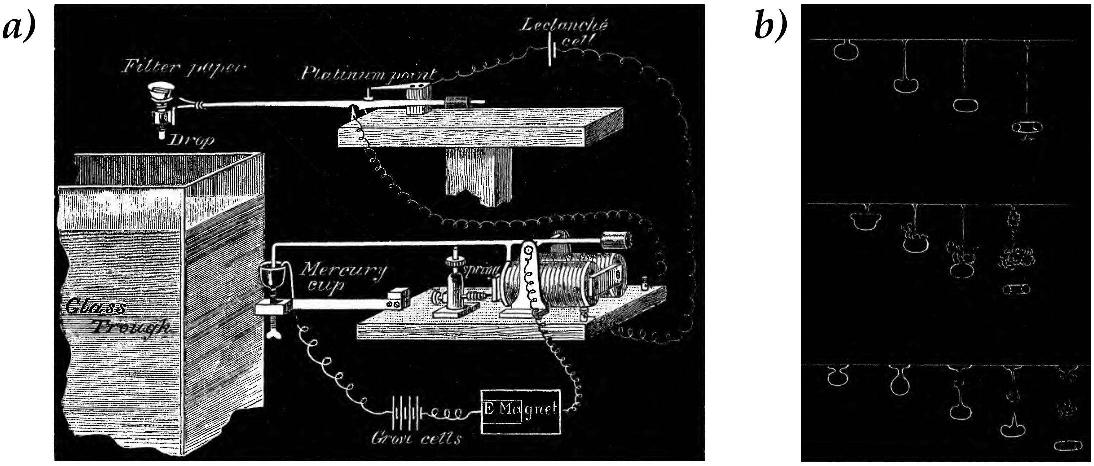

Figure 1.2: *Sketches from* ***a***) *J.J. Thomson's experimental setup to study coalescence, and* ***b***) *vortex formation during the engulfment process. Adapted from Thomson and Newall, 1886.*

drop pinch-off, where a liquid thread narrows progressively until its radius vanishes (Figure 1.1c). These singular phenomena are a hallmark of nonlinear partial differential equations and appear in diverse fields including turbulence (Passot et al., 1995), gravitation (Volonteri et al., 2021), biological growth (Childress and Percus, 1981), and even financial market dynamics (Sornette and Johansen, 1997). Near such singularities, the governing equations often exhibit rich, multiscale dynamics characterized by self-similar and, in many cases, universal behavior.

The first identification of self-similarity in free surface flows was made by Keller (1983), who studied retracting sheets and threads of inviscid fluids. Over the past four decades, self-similar dynamics have been uncovered in a wide range of interfacial phenomena, including the rupture of liquid threads (Eggers, 1993; Day et al., 1998), the breakup of liquid sheets (Zhang and Lister, 1999), the coalescence of liquid drops (Eggers et al., 1999; Kaneelil et al., 2022), and the merging of gas bubbles in liquids (Munro et al., 2015). The emergence of self-similarity reveals the dominant physical mechanisms at play and enables the formulation of scaling laws that describe the intermediate asymptotic behavior of the system. In cases of universality, these scaling laws are independent of the initial or boundary conditions, reflecting an inherent symmetry of the underlying dynamics. From the perspective of nonlinear dynamics, such universal scaling regimes correspond to attractors or fixed points, defined by a balance between the primary driving and dissipative forces in the system (Eggers and Fontelos, 2008).

1.2 Drop Coalescence

The coalescence of liquid drops or other fluid volumes is a fundamental topological transition in free surface flows, complementary to breakup (Eggers et al., 2024). The earliest systematic study of this phenomenon dates back to Thomson and Newall (1886), who investigated drops coalescing onto a bath and observed vortex forma-

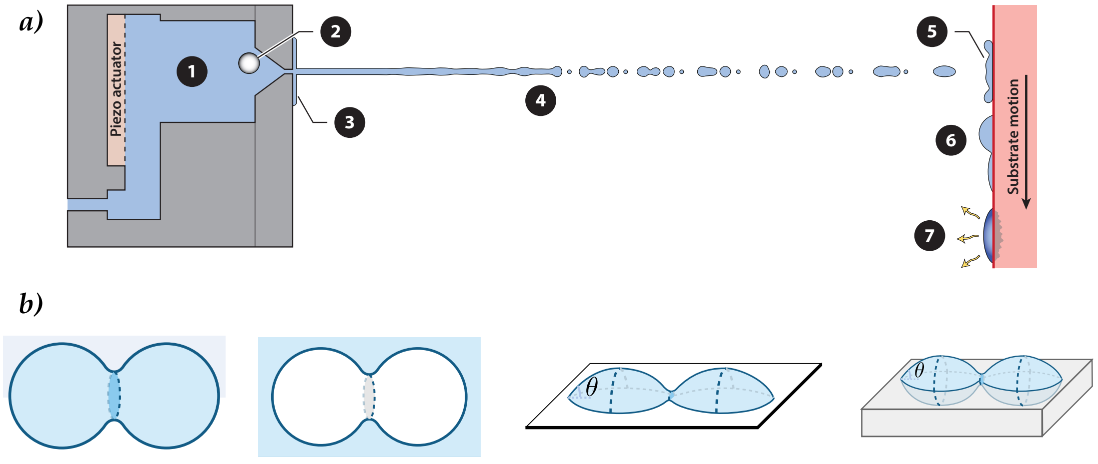

i) Drops ii) Bubbles iii) Sessile drops iv) Liquid lenses

Figure 1.3: ***a***) *Visualization of series of events in inkjet printing. The circled numbers refer to the seven fundamental fluid dynamics challenges referenced in Lohse (2022). In this work,* ⑥ *process is studied where drops interact with other drops on the substrate.* ***b***) *Various geometries for coalescence where we focus on setup iii) Sessile drops. Adapted from Eggers et al. (2024)*

tion during the engulfment process. These events occur near singularities, where the formation of new structures like drops takes place and rapid motion imprints strong dynamical signatures. The vicinity of such singularities is of special physical and technological relevance, often displaying a simplified, self-similar structure. This simplification makes the problem more tractable analytically despite the inherent nonlinearity and complexity of the governing equations. Coalescence plays a key role in various industrial applications such as in emulsions (Chesters, 1991), oil recovery (Kavehpour, 2015), inkjet printing (Lohse, 2022), and the collision of dispersed particles (Liao and Lucas, 2010). Coalescence modeling has also extended into biology to describe the merging of cell nucleoli and multicellular aggregates (Pokluda et al., 1997; Caragine et al., 2018).

In coalescence, the motion begins in the singular regime, where the geometry is fully determined by the initial conditions. Unlike breakup, where the dynamics often converge to universal scaling laws regardless of geometry, coalescence dynamics remain sensitive to the imposed shape and configuration. An additional layer of complexity arises from the influence of the outer fluid. Even when the outer phase is of negligible viscosity, it can significantly affect the dynamics due to confinement within the narrow gap between the approaching interfaces. In such cases, lubrication effects become dominant and must be taken into account (Davis et al., 1989; Sprittles, 2024).

A comprehensive understanding of drop coalescence necessitates a breakdown of the process into distinct stages. First, during the approach phase, two drops come into proximity, resulting in formation of a small bridge. The coalescence dynamics here depend non-universally on the impact speed. At small separations, thin-film drainage and lubrication forces, amplified by rarefied gas effects, become dominant. The second stage is reconnection, where microscopic interactions (e.g., van der Waals forces or electrostatics) lead to the actual contact or ”jump-to-contact” before geometric overlap. The third stage is coalescence where the initial dynamics are driven by surface tension. A rapidly expanding liquid bridge forms, localized near the meniscus. Although this region follows scaling laws, deviations such as logarithmic corrections are often observed, and self-similarity is not guaranteed (Eggers et al., 1999; Paulsen, 2013). Finally, in the merging stage, the bulk of the original drops mix to form a unified drop. Most of the mass transfer occurs here as the drops lose their identity. This stage is essential for applications requiring homogenization and has been analyzed in both experimental and theoretical settings (Ashgriz and Poo, 1990; Verdier, 2001).

1.3 Surfactants

‘Surface-active’ molecules and/or particles, collectively called ‘surfactants’, control the initiation, dynamics and behaviour of many natural processes and industrial applications. Surfactants consist of a hydrophobic tail and a hydrophilic head (Kresheck, 1975). Their presence at the interface introduces an additional surface excess pressure, ultimately reducing the surface tension of the liquid. One key effect of surfactants is the generation of Marangoni stresses, which arise from surface tension gradients. These stresses generally act to oppose interfacial flows and can effectively rigidify the interface. As a result, surfactants influence a wide range of interfacial phenomena, including film coatings (Shen et al., 2002; Hofsäss and Zhang, 2008), thin films (Temprano-Coleto and Stone, 2024; Eshima et al., 2024), and the dispersion of surface waves (Ceniceros, 2003; Sauleda et al., 2022).

The physical manifestation of surfactants extends beyond simple surface tension reduction. Historical observations of these effects include the “tears of wine” phenomenon, where a liquid film climbs along the wall of a wine glass, evaporates, and drips tiny droplets due to Marangoni stresses (Hosoi and Bush, 2001; de Gennes et al., 2003). In industrial context, surfactants enable processes ranging from electrospray formation from Taylor cones (Taylor, 1964; Ashgriz, 2011) to the stabilization of Leidenfrost drops on superheated surfaces (Boerhaave, 1732; Leidenfrost, 1756; Quéré, 2013). These diverse applications underscore the fundamental role of surfactants in controlling interfacial dynamics across multiple scales and physical regimes.

The coupling between surfactants and hydrodynamics typically occurs through surfactant isotherms depicting the relationship between interfacial tension and surfactant concentration. Some of the most common models are shown in Table 1.1. The simplest model, Henry’s isotherm, assumes a linear relationship, while more complex models like Langmuir, Frumkin, and van der Waals isotherms capture nonlinear effects including saturation and intermolecular interactions. These constitutive relations serve as closure conditions for the coupled hydrodynamic-surfactant transport problem.

Table 1.1: *Overview of various adsorption isotherms with corresponding source terms and surface pressures*

Isotherm	$\mathcal{S}_\Gamma^{\text{ads}}$	$\mathcal{S}_\Gamma^{\text{des}}$	Π
Henry Isotherm	$k_{\text{ads}}C$	$k_{\text{des}}\Gamma$	$RT\Gamma$
Langmuir Isotherm	$k_{\text{ads}}C\dfrac{\Gamma_\infty - \Gamma}{\Gamma_\infty}$	$k_{\text{des}}\Gamma$	$-RT\Gamma_\infty \ln\left(1 - \dfrac{\Gamma}{\Gamma_\infty}\right)$
Volmer Isotherm	$k_{\text{ads}}C\dfrac{\Gamma_\infty - \Gamma}{\Gamma_\infty}$	$k_{\text{des}}\Gamma \exp\left(\dfrac{\Gamma}{\Gamma_\infty - \Gamma}\right)$	$\dfrac{RT\Gamma_\infty}{1 - \Gamma/\Gamma_\infty}$
Frumkin Isotherm	$k_{\text{ads}}C\dfrac{\Gamma_\infty - \Gamma}{\Gamma_\infty}$	$k_{\text{des}}\Gamma \exp\left(-\dfrac{\beta\Gamma}{RT}\right)$	$-RT\Gamma_\infty \ln\left(1 - \dfrac{\Gamma}{\Gamma_\infty}\right)$
Van Der Waals Isotherm	$k_{\text{ads}}C\dfrac{\Gamma_\infty - \Gamma}{\Gamma_\infty}$	$k_{\text{des}}\Gamma \exp\left(\dfrac{\Gamma}{\Gamma_\infty - \Gamma} - \dfrac{\beta\Gamma}{RT}\right)$	$\dfrac{RT\Gamma_\infty}{1 - \Gamma/\Gamma_\infty} - \dfrac{\beta\Gamma^2}{2}$

1.4 Drop Coalescence in Presence of Surfactants

The coalescence of Newtonian droplets has been extensively studied over the past five decades and is now well understood (Eggers et al., 2024). Capillary forces drive the rapid growth of the liquid bridge connecting the drops, eventually merging them into a single fluid body. However, when sessile drops composed of two different but miscible liquids come into contact, immediate coalescence is not always observed. Under specific conditions, the liquid bridge remains thin compared to the droplet sizes, and the two drops remain connected via a neck while moving across the substrate. In this regime, the droplet with lower surface tension actively pursues the one with higher surface tension, with full merging occurring only after a considerable delay.

The underlying mechanism behind this *delayed coalescence* is the interplay between capillary-driven and Marangoni-driven flows (Karpitschka and Riegler, 2012; Karpitschka and Riegler, 2014). A surface tension gradient between the droplets induces a Marangoni flow that counteracts the capillary-induced neck growth by draining the bridge region. When the Marangoni flow is sufficiently strong, it not only suppresses bridge expansion but also causes the neck to migrate toward the higher-surface-tension droplet. This creates the striking phenomenon of *twin-drop* motion, where connected drops chase each other across the substrate while maintaining a thin connecting bridge.

A systematic experimental study by Bruning et al. (2018) explored the coalescence behavior of sessile drops containing surfactant solutions, revealing that surfactant-induced Marangoni stresses significantly alter the coalescence dynamics. They identified three distinct non-coalescence modes and demonstrated that the process depends intricately on surfactant concentration—beyond what can be explained by surface tension difference alone. Despite these insights, the initial bridge scaling and its early-stage dynamics remain poorly understood, particularly how surfactants modify the hydrodynamic singularity at contact.

Recent observations of similar phenomena in natural systems, from raindrop coalescence on leaves (Kim et al., 2020; Lohse and Villermaux, 2020) to bubble dynamics in contaminated liquids, suggest that surfactant-mediated coalescence is ubiquitous.

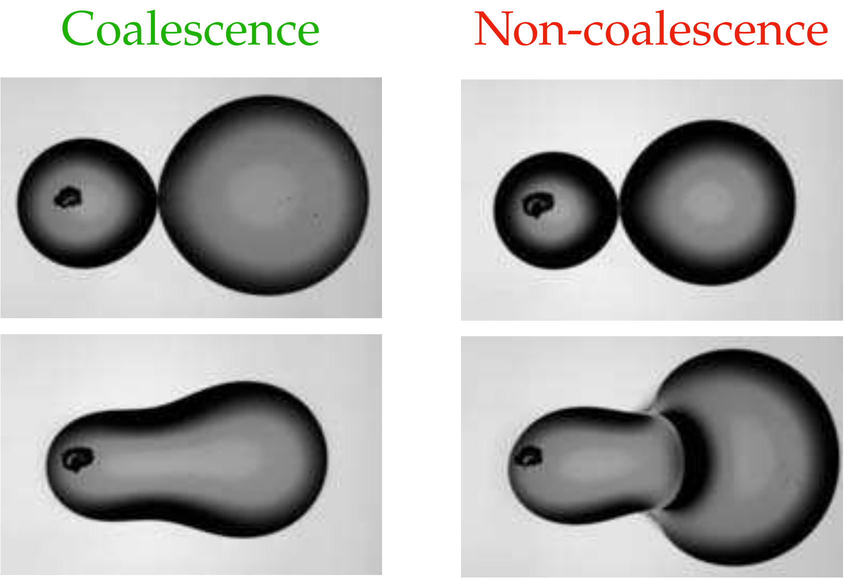

Figure 1.4: *Experimental comparison between coalescence and non-coalescence of two liquid drops. In the coalescence case, there exists no difference in surface tension and the smaller drop merges fully with the larger one. In contrast, during non-coalescence, the binary drops show a non-coalescent twin drop movement [Adapted from Karpitschka and Riegler (2012)].*

The challenge lies in understanding how the microscale physics near the singularity – where continuum assumptions may break down – connects to the macroscale observations of delayed coalescence and non-coalescent motion. This multiscale coupling, mediated by surfactant transport and Marangoni stresses, forms the central focus of our investigation.

1.5 Guide Through the Thesis

This thesis is organized as follows. In Chapter 2, we present the overall problem formulation, introduce the governing equations, and identify the key dimensionless parameters that govern the dynamics. The chapter concludes with a brief description of the numerical scheme employed to solve the coupled system.

We then proceed to Chapter 3, where we explore the early-stage dynamics of coalescence in the low-Pe regime, characterized by dominant surfactant diffusion. Here we introduce the concept of a temporal boundary layer and derive analytical scaling laws for both vertical and horizontal bridge motion.

Chapter 4 serves as an interlude, focusing on the maximum horizontal displacement of the neck. It highlights how the dynamics begin to shift as we transition toward higher Pe values, revealing non-trivial behavior and the emergence of a critical surfactant strength.

In Chapter 5, we delve into the high-Pe regime in greater detail. Here, we investigate the rich and often counterintuitive dynamics arising from strong Marangoni stresses, including vorticity generation and shock formation. This chapter reveals how surfactants can fundamentally alter or even arrest the coalescence singularity.

The thesis concludes with Chapter 6, where we summarize the key findings and outline potential directions for future research. Lastly, Chapter 7 provides access to the GitHub repository containing all simulation codes used in this study, which are open-source and freely available.

2

Methodology

This chapter formulates the physical problem, derives the governing equations, and outlines the numerical method to solve the physical problem.

2.1 Problem Formulation

Figure 2.1 shows the physical setup: two viscous sessile drops with identical viscosity μ placed on a planar substrate. The drops contact at an initial angle θ, with characteristic radius L and height H.

For small gravitational effects (low Bond number), the drops form spherical caps with

$$H = \frac{L}{\sin\theta}(1 - \cos\theta). \tag{2.1}$$

For small contact angles ($\theta \ll 1$), a first-order Taylor expansion gives $\theta \approx 2H/L$. A precursor film of thickness $h_\infty \sim \mathcal{O}(10^{-4})L$ initially separates the drops. Alternatively, a pre-formed liquid bridge of comparable dimensions can be used to initiate

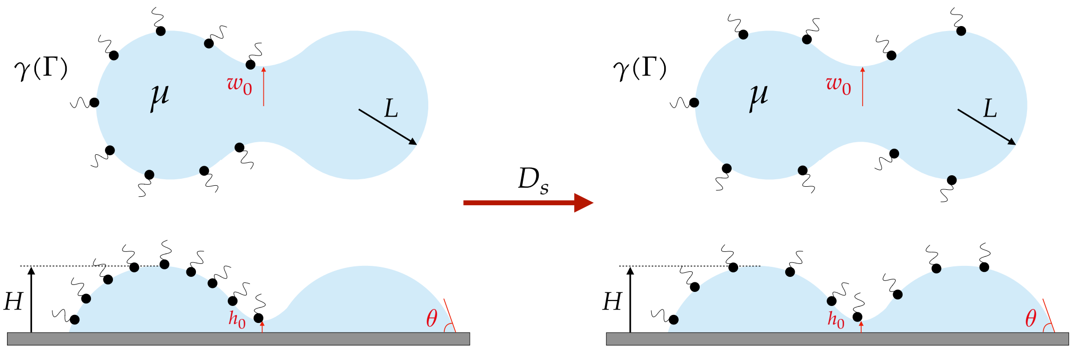

Figure 2.1: *Schematic representation of the initial and intermediate stages of surfactant-mediated coalescence between two viscous drops. The left drop is initially laden with surfactants, while the right drop remains surfactant-free. Surfactants diffuse along the interface with a surface diffusion coefficient* D_s*. Both drops have the same viscosity* μ*, characteristic radius* L*, and contact angle* θ*. The neck height is denoted by* h_0 *while* w_0 *denotes the width of the bridge.*

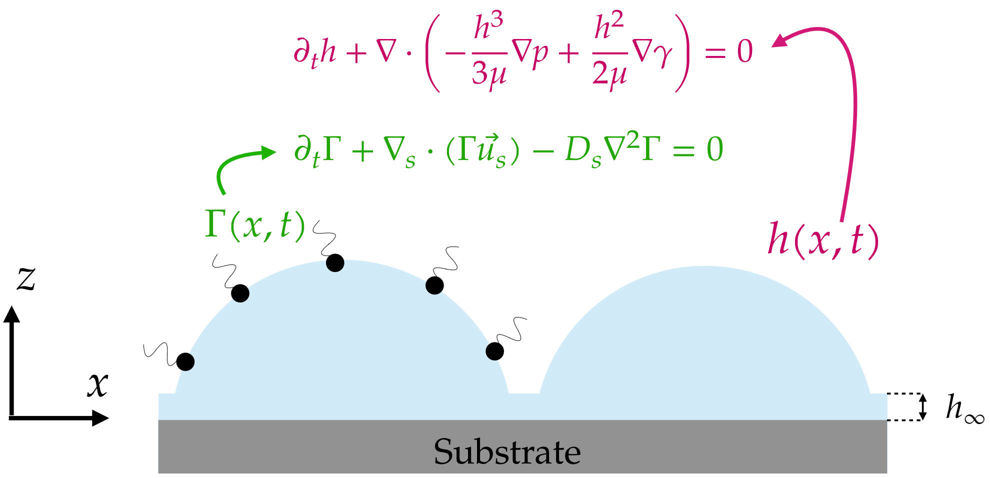

Figure 2.2: *Schematic of the two-dimensional lubrication model incorporating surfactant transport. The figure illustrates the film height profile $h(x,t)$ and interfacial surfactant concentration $\Gamma(x,t)$. A thin precursor film of thickness h_∞ regularizes the contact line singularity.*

contact; however, no appreciable difference in the early-time dynamics is observed between the two configurations. At the non-coalescing side of the drops, the precursor film also regularizes the contact line singularity while maintaining negligible spreading rates during the early-time dynamics of interest (Hernández-Sánchez et al., 2012). While the precursor film influences long-time spreading behaviour, we focus only on early-time dynamics when the slow spreading contribution can be safely ignored (Hernández-Sánchez et al., 2012).

Surfactants are introduced solely in the left drop and in the adjacent precursor film. The precursor film is pre-laden with surfactants such that the diffusive flux from the drop to the film remains minimal compared to the interfacial transport towards the right drop. The left drop is uniformly coated with surfactants at an initial interfacial concentration Γ_0. These surfactants undergo surface diffusion along the interface, characterized by a diffusion coefficient D_s. Although D_s may in general depend on the local surfactant concentration Γ (Saffman and Delbrück, 1975; Manikantan and Squires, 2020), we assume it to be constant for this study.

The interfacial tension γ varies smoothly with the local surfactant concentration Γ. We adopt Henry's isotherm, which postulates a linear dependence between surface tension and surfactant concentration.

2.2 Governing Equations

Given the viscous nature of the fluid and small contact angles, we adopt the lubrication approximation. We consider a two-dimensional configuration where drops are approximated as infinitely long cylinders. This assumption is appropriate at early times, where three-dimensional coalescence dynamics follow the same asymptotic behavior as the two-dimensional counterpart (Eggers et al., 1999).

More recently, Kaneelil et al. (2022) demonstrated that the three-dimensional interface evolution exhibits a self-similar form that projects onto a universal curve also captured by a two-dimensional description. However, surfactant transport along the interface may show dimensional dependence. The diffusion and redistribution of surfactants in three dimensions is expected to deviate from two dimensions. Nonetheless, as a leading-order approximation, the two-dimensional framework provides a reasonable description of the system.

To model the coalescence dynamics, we couple the lubrication equation with the surfactant transport equation describing interfacial advection and diffusion (Oron et al., 1997; Craster and Matar, 2009). This framework captures the interplay between hydrodynamic flow and surface concentration gradients arising from Marangoni stresses. Detailed derivations are provided in Appendix A and Appendix B.

The evolution equation for film height under the lubrication approximation is

$$\partial_t h + \nabla \cdot \left(-\frac{h^3}{3\mu} \nabla p + \frac{h^2}{2\mu} \nabla \gamma \right) = 0, \tag{2.2}$$

where the first divergence term represents pressure-driven Poiseuille flow, while the second captures Marangoni flow due to surface tension gradients (Thiele et al., 2012). The pressure p relates to interface curvature and surface tension through the normal stress balance,

$$p + \nabla \cdot (\gamma \nabla h) = 0. \tag{2.3}$$

Here, $h = h(x, t)$ denotes the local film thickness, p is the pressure, γ is the surface tension, and μ is the dynamic viscosity. Temporal and spatial partial derivatives are denoted by ∂_t and ∂_x, respectively, while the planar gradient operator is defined as $\nabla = (\partial_x, \partial_y)$.

The temporal evolution of interfacial surfactant concentration $\Gamma(x, t)$ follows a surface advection-diffusion equation,

$$\partial_t \Gamma + \nabla_s \cdot (\Gamma \vec{u_s}) - D_s \nabla^2 \Gamma = 0, \tag{2.4}$$

where D_s denotes the surface diffusion coefficient and $\vec{u_s}$ is the tangential velocity along the interface.

The surface gradient operator ∇_s projects the spatial gradient onto the local tangent plane: $\nabla_s = (\underline{\mathbf{I}} - \mathbf{nn}) \cdot \nabla$, where $\underline{\mathbf{I}}$ is the identity tensor and $\mathbf{n}$ is the unit normal vector to the free surface.

For low surfactant coverage, the constitutive relation for surface tension is

$$\gamma = \gamma_0 - a\Gamma, \qquad 0 < \Gamma < \Gamma_\infty, \tag{2.5}$$

where γ_0 denotes the surface tension of a clean interface, and $a = \|\partial\gamma/\partial\Gamma\|$ is the surfactant strength modulus representing sensitivity of surface tension to surfactant concentration variations, and Γ_∞ denotes the saturation limit beyond which the linear model becomes invalid.

In the present study, we operate strictly within the regime where $\Gamma(x,t)$ remains below the saturation threshold Γ_∞ for all space and time.

Substituting the linear equation of state (Equation (2.5)) into the height evolution and surfactant transport equations yields the fully coupled system,

$$\partial_t h + \nabla \cdot \left(-\frac{h^3}{3\mu}\nabla p - \frac{a h^2}{2\mu}\nabla\Gamma \right) = 0, \tag{2.6}$$

$$p + \nabla \cdot (\gamma_0 \nabla h - a\Gamma\nabla h) = 0, \tag{2.7}$$

$$\partial_t \Gamma + \nabla \cdot \left(-\frac{a h \Gamma}{\mu}\nabla\Gamma - \frac{h^2\Gamma}{2\mu}\nabla p - D_s\nabla\Gamma \right) = 0. \tag{2.8}$$

We assume the surface gradient operator ∇_s may be approximated by the planar gradient ∇, valid in the lubrication limit for small contact angles. The interfacial velocity u_s is approximated by the horizontal component of bulk velocity, $u_x|_{z=h}$, justified by the drop geometry.

2.2.1 Non-Dimensional Parameters

We non-dimensionalize equations (2.6), (2.7), and (2.8) using:

$$h \longrightarrow L\tilde{h}, \quad x \longrightarrow L\tilde{x}, \quad y \longrightarrow L\tilde{y}, \quad p \longrightarrow \left(\frac{\gamma_0}{L}\right)\tilde{p}, \quad t \longrightarrow \left(\frac{L}{\mathcal{U}}\right)\tilde{t}, \quad \Gamma \longrightarrow \Gamma_\infty\tilde{\Gamma},$$

where $\mathcal{U} = \gamma_0/\mu$ is the characteristic viscocapillary velocity scale arising from balance between surface tension and viscous forces, setting the natural timescale $L/\mathcal{U}$.

Both vertical film height h and horizontal coordinate x are rescaled using drop radius L, removing dependence on aspect ratio H/L which scales with contact angle θ. The governing equations reduce to

$$\partial_{\tilde{t}}\tilde{h} + \tilde{\nabla} \cdot \left(-\frac{\tilde{h}^3}{3}\tilde{\nabla}\tilde{p} - \beta\frac{\tilde{h}^2}{2}\tilde{\nabla}\tilde{\Gamma} \right) = 0, \tag{2.9}$$

$$\tilde{p} + \tilde{\nabla} \cdot \left(\tilde{\nabla}\tilde{h} - \beta\tilde{\Gamma}\tilde{\nabla}\tilde{h} \right) = 0, \tag{2.10}$$

$$\partial_{\tilde{t}}\tilde{\Gamma} + \tilde{\nabla} \cdot \left(-\beta\tilde{h}\tilde{\Gamma}\tilde{\nabla}\tilde{\Gamma} - \frac{\tilde{h}^2}{2}\tilde{\Gamma}\tilde{\nabla}\tilde{p} - \frac{1}{Pe}\tilde{\nabla}\tilde{\Gamma} \right) = 0, \tag{2.11}$$

For brevity, we omit the tildes $(\tilde{\cdot})$ from this point onwards.

- The surfactant strength number β quantifies the strength of surfactant-induced surface tension gradients relative to clean surface tension:

$$\beta = \frac{a\Gamma_\infty}{\gamma_0}.$$

- The surface Péclet number Pe is the ratio of advective to diffusive transport along the interface:

$$Pe = \frac{\mathcal{U}L}{D_s} = \frac{\gamma_0 L}{\mu D_s}.$$

We note that the contact angle θ does not explicitly appear in the dimensionless equations, a direct consequence of scaling both horizontal and vertical coordinates with the same characteristic length L. Table 2.1 summarizes all relevant dimensionless parameters.

Table 2.1: *List of dimensionless parameters involved in the problem*

Dimensionless parameter		Description
Pe (Péclet number)	$Pe = \frac{\gamma_0 L}{\mu D_s}$	Ratio of advection to difussion of the surfactants
β (Surfactant strength)	$\beta = \frac{a\Gamma_\infty}{\gamma_0}$	Rate of change of surface tension with surfactant concentration
θ (Contact angle)	$\theta \approx \frac{2H}{L}$	Initial angle of contact between drops

2.3 Numerical Scheme

The system of Equations (2.9)–(2.11) is solved using the finite element package PYOOMPH (Diddens and Rocha, 2024), built on OOMPH-LIB (Heil and Hazel, 2006) with symbolic computations via GiNaC (Christian Bauer and Kreckel, 2002). The computational domain is discretised with a one-dimensional mesh of line elements. The scalar fields h, p, and Γ are represented using quadratic, continuous Lagrangian shape functions. Time integration employs a second-order backward differentiation formula (BDF2).

At each time step, the residual vector is assembled from the discretised system. The Jacobian and mass matrices are computed. An implicit monolithic method solves the resulting nonlinear system, iteratively updating the solution until convergence.

We perform simulations for various combinations of $\{\beta, Pe, \theta\}$. The initial concentration on the left drop is fixed at $\Gamma_0 = 0.8$ and the initial contact angle is 20°, unless otherwise stated.

3

Drop coalescence: Low Pe limit

This chapter examines the limit of $Pe \ll 1$ where surfactant transport is dominated by diffusion.

3.1 Evolution of the Drop Height

Figure 3.1 illustrates the temporal evolution of the bridge during the coalescence process for a system with surfactant strength number $\beta = 0.1$ and surface Péclet number $Pe = 1$. The *bridge* refers to the connecting liquid region between the two initially distinct drops, while the *neck* denotes the location of minimum film thickness $r = h(t)$ within the bridge.

The top interface is color-coded to show the interfacial surfactant concentration Γ. At low Péclet number, the surfactant profile rapidly diffuses along the interface, creating spatially uniform surface tension over a short timescale. The characteristic diffusion time scales as L^2/D_s. Compared to the viscocapillary timescale $L\mu/\gamma_0$, uniform surface tension is achieved at timescale $\mathcal{O}(Pe)$. Since $Pe = 1$, the plots show times $t \gg t_d$, where t_d denotes the time for complete surfactant homogenization.

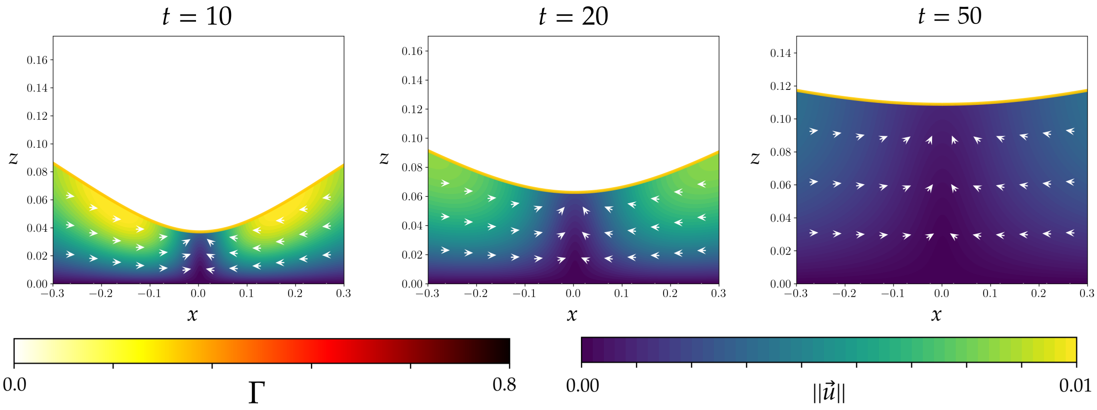

Figure 3.1: *Time evolution of the drop bridge for $\beta = 0.1$, $Pe = 1$ and $\theta = 20°$, showing the surfactant concentration $\Gamma(x,t)$ (colormap at the top interface) and velocity magnitude $||\vec{u}||$ (background colormap), overlaid with velocity vectors.*

In this regime, Marangoni stresses vanish due to uniform Γ, and flow is driven purely by Laplace pressure gradients. The large negative curvature at the neck creates significantly lower capillary pressure compared to the adjoining drops. This pressure imbalance drives fluid motion from the bulk drops into the bridge region, promoting growth. The flow field, shown via velocity vectors, reflects this influx, resulting in complete coalescence as the bridge radius approaches that of the initial drops. At sufficiently long times, the system behaves analogously to classical coalescence of Newtonian drops without surfactants.

3.1.1 Early-Time Behavior

To investigate dynamics during initial coalescence stages, we perform simulations in the regime $t < t_d$, where Marangoni stresses dominate. Figure 3.2 shows the results. At $t = 0.1$, the surfactant concentration along the interface is highly non-uniform, creating surface tension gradients. Lower surfactant concentrations near the right drop lead to higher surface tension in that region. This gradient drives Marangoni flow toward the right, evident in the velocity vectors at $t = 0.1$.

As time progresses, interfacial diffusion flattens the surfactant profile, weakening Marangoni stresses. Around $t = 1.0$, surfactant diffusion is nearly complete, and Laplace pressure from neck curvature begins dominating the dynamics. This causes pressure-driven flow toward the bridge region, gradually reorienting the velocity field. By $t = 2.0$, the surfactant distribution is nearly uniform, and the system transitions to flow governed solely by capillary pressure gradients. The velocity field now shows symmetric inflow from both sides toward the neck.

Notably, the observed diffusive relaxation timescale aligns with the expected value $t_d \sim \mathcal{O}(Pe)$. Since $Pe = 1$, the flattening of the surfactant profile around $t \approx 1.0$ is consistent with theoretical predictions.

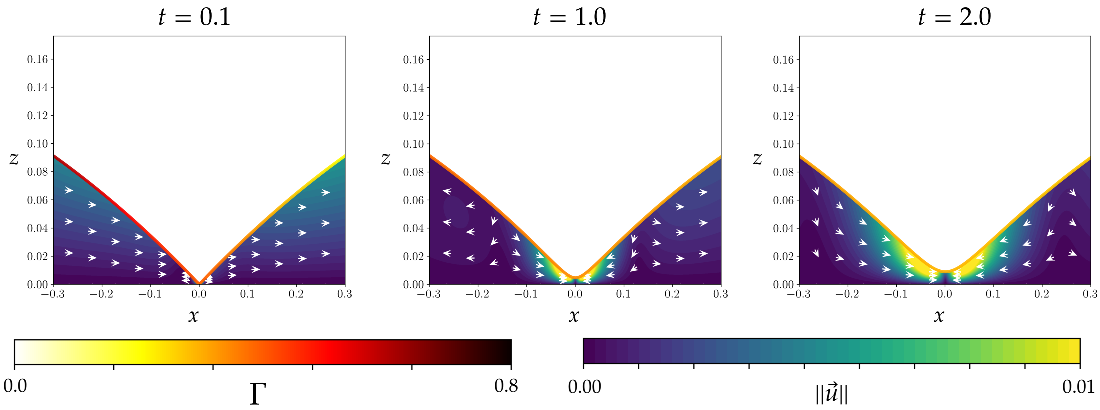

Figure 3.2: *Early-time evolution of the drop interface for $\beta = 0.1$, $\theta = 20°$ and $Pe = 1$. The surfactant concentration $\Gamma(x, t)$ is shown along the interface, while the background colormap and arrows represent the velocity magnitude $\|\vec{u}\|$ and flow direction, respectively. At $t = 0.1$, strong Marangoni stresses drive flow toward the right drop, where surface tension is higher. As time progresses, surfactant diffusion smooths out the concentration profile, diminishing the Marangoni effect.*

3.1.2 Diffusive Time Scale and the Temporal Boundary Layer

To better understand the early-time dynamics of surfactant transport, we introduce a *temporal boundary layer*. This construct is analogous to classical spatial boundary layers in fluid mechanics, originally proposed by Prandtl (Anderson, 2005), illustrated schematically in Figure 3.3a). The horizontal axis represents the Péclet number Pe, while the vertical axis denotes time t.

Within this framework, surfactant redistribution evolves rapidly over a narrow temporal region near $t = 0$, forming a diffusive boundary layer in time. Figure 3.3b) shows the temporal evolution of a representative surfactant concentration profile $\Gamma(x, t)$. The initially non-uniform profile diffuses toward a spatially uniform distribution. Beyond the boundary layer, concentration equilibrates to a uniform value given by the spatial average, $\Gamma = \int \Gamma \, dx / \int dx = \Gamma_0/2$.

We further characterize the thickness δ of this temporal boundary layer in terms of Pe. The relevant time scales are the convection time scale $t_c = L\mu/\gamma_0$ and the diffusion time scale $t_d = L^2/D_s$. This gives $t_d = Pe \cdot t_c$, suggesting that the temporal boundary layer extent scales as $\delta \sim Pe$.

In the asymptotic limit $Pe \to 0$, we find $t_c \gg t_d$, indicating diffusion-dominated dynamics. Hence, modeling the system using a temporal boundary layer approximation captures early-time surfactant transport behavior.

We stress that the relevant advective-diffusive balance near the bridge region is governed not by the global Péclet number Pe, but by a *local* Péclet number, Pe_{local} (Equation 3.1). This distinction arises because the characteristic length scale in the neck is much smaller than the overall drop radius L, requiring localized scaling for transport dynamics.

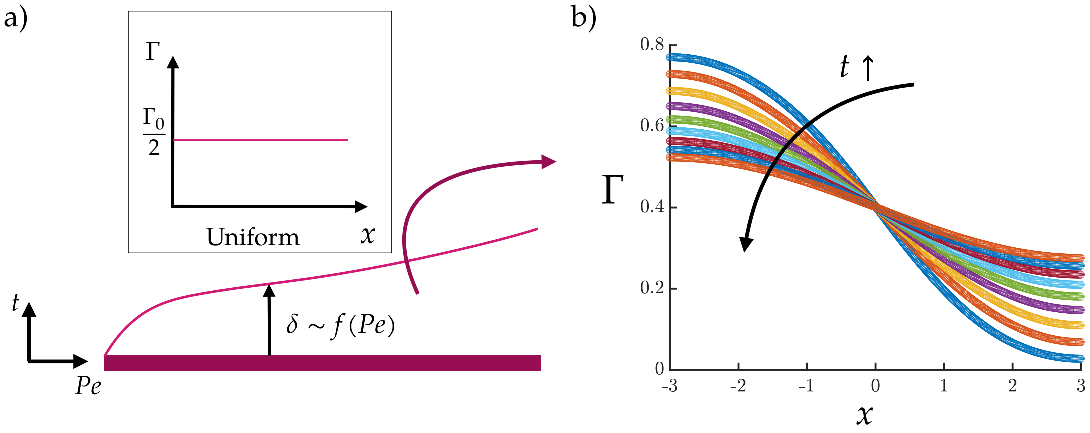

Figure 3.3: *(a) Schematic illustration of the temporal boundary layer. The boundary layer thickness δ scales with the Péclet number as $\delta \sim f(Pe)$, and beyond this layer, the surfactant concentration Γ becomes uniform with an average value $\Gamma_0/2$. (b) Temporal evolution of the interfacial surfactant concentration $\Gamma(x, t)$ for a representative case.*

We define the local Péclet number as

$$Pe_{\text{local}} = \frac{L_{\text{local}}}{L} Pe, \tag{3.1}$$

where L_{local} represents the characteristic length scale in the neck region. We identify L_{local} with the precursor film thickness h_∞, chosen as $h_\infty/L = \mathcal{O}(10^{-4})$. Substituting this into the expression for Pe_{local} gives

$$\frac{Pe_{\text{local}}}{Pe} = \mathcal{O}(10^{-4}),$$

implying that local surfactant dynamics evolve over a much faster diffusive timescale than predicted by the global Péclet number. This highlights the need to account for strong scale separation when analyzing early-time interfacial flows in the neck region.

Given that $Pe_{\text{local}} \ll 1$, we expand the dependent variables h and Γ in regular asymptotic series in powers of Pe,

$$h = h_0 + Pe \cdot h_1 + \mathcal{O}(Pe^2),$$

$$\Gamma = \Gamma_0 + Pe \cdot \Gamma_1 + \mathcal{O}(Pe^2)$$

Substituting these perturbation expansions into the governing equations for film height and surfactant concentration, we collect terms at each order of Pe to obtain a series of linear evolution equations describing dynamics at leading and higher orders. The resulting system of equations is analyzed in the following section.

3.2 Theory

3.2.1 Surfactant Profile

Figure 3.3b) shows the evolution of interfacial surfactant concentration $\Gamma(x,t)$ over time for $\beta = 0.1$, $\theta = 20°$ and $Pe = 1$. At early times, the surfactant profile is highly non-uniform, but diffuses toward a uniform state as time progresses. To analyze this behavior theoretically, we consider a leading-order asymptotic approximation in the limit $Pe_{\text{local}} \ll 1$, as previously justified. Under this assumption, the nonlinear advective term $\nabla_s \cdot (\Gamma u_s)$ in the surfactant transport equation is negligible. The governing equation for the leading-order surfactant profile reduces to a one-dimensional linear diffusion equation:

$$\frac{\partial \Gamma}{\partial t} - \frac{1}{Pe}\frac{\partial^2 \Gamma}{\partial x^2} = 0. \tag{3.2}$$

As an initial condition, we consider a sharp interfacial discontinuity in surfactant concentration, with the left drop initially saturated at $\Gamma = \Gamma_0$ and the right drop surfactant-free. Accordingly, the initial profile is:

$$\Gamma(x,0) = \begin{cases} \Gamma_0, & x < 0, \\ 0, & x > 0. \end{cases}$$

This step function captures the initial configuration and allows analytical solution of Equation (3.2), giving

$$\Gamma(x,t) = \frac{\Gamma_0}{2}\left(1 - \operatorname{erf}\left(\frac{Pe^{1/2}x}{2t^{1/2}}\right)\right),$$

where the error function is defined as

$$\operatorname{erf}(z) = \frac{2}{\sqrt{\pi}}\int_0^z e^{-t^2}\,dt.$$

This closed-form solution is derived using the method of Laplace transforms, as detailed in Crank (1979). This expression for $\Gamma(x,t)$ is to be used in subsequent steps to evaluate the corresponding film height $h(x,t)$ and horizontal velocity field, as discussed in the following sections.

3.2.2 Height Profile

Figure 3.4 presents the temporal evolution of the neck height $h_0(t)$ as a function of time for various combinations of the dimensionless parameters β, Pe, and θ. At early times, the neck height exhibits a linear growth with time, i.e., $h_0 \propto t$, as indicated by the black reference slope. This scaling behavior is consistent with asymptotic results for viscous drop coalescence (Eggers et al., 1999; Aarts et al., 2005), and holds even with surfactants present.

At later times, however, the linear scaling begins to break down as the neck grows to a size comparable to the drop radius. Eventually, the height saturates and approaches a steady value, with the two drops merging into one.

In addition to confirming the scaling behavior, Figure 3.4 reveals that despite variations in β and Pe, the data collapse into two distinct groups corresponding to different contact angles: blue-shaded points for $\theta = 10°$ and green-shaded points for $\theta = 20°$. This suggests neck height h_0 is largely insensitive to surfactant strength number β and Péclet number Pe, but strongly depends on contact angle θ.

Film height evolution is governed by two primary contributions: capillary flux $\left(\frac{h^3}{3}\nabla p\right)$, driving vertical flow from curvature-induced pressure gradients, and Marangoni flux $\left(\beta\frac{h^2}{2}\nabla\Gamma\right)$, arising from surface tension gradients and acting primarily horizontally. While the Marangoni term is directed along the interface, it contributes to vertical interface evolution due to finite contact angle θ, which projects a horizontal gradient into a component normal to the surface.

Despite this coupling, at early times, we invoke the leading-order asymptotic ap-

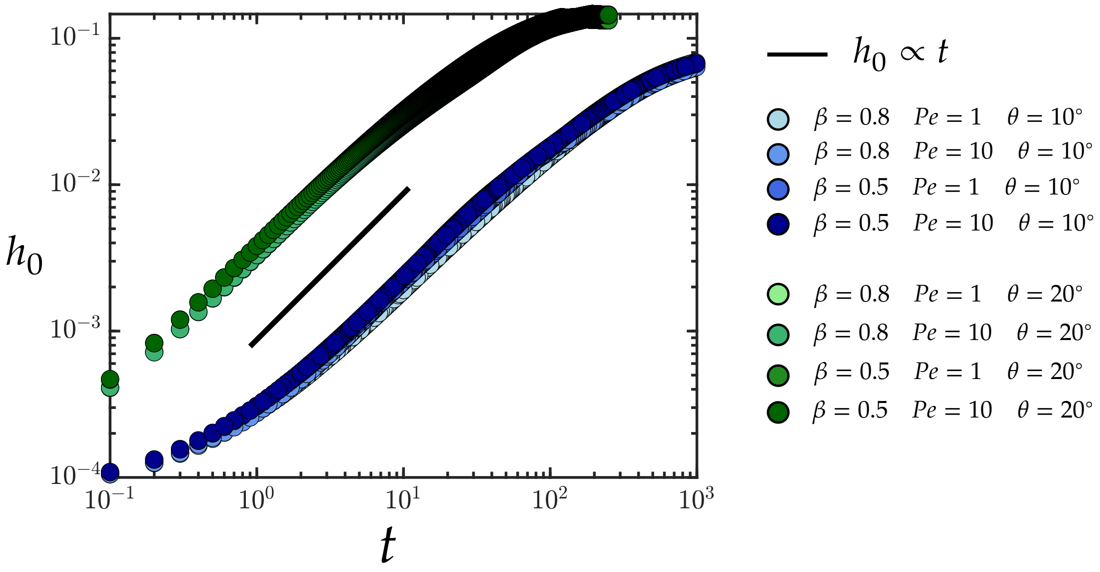

Figure 3.4: *Temporal evolution of the neck height h_0 for various combinations of β, Pe, and contact angle θ. The black reference line indicates linear scaling $h_0 \propto t$ at early times, consistent with theoretical predictions for viscous drop coalescence.*

proximation in the limit $Pe_{\text{local}} \ll 1$. Under this expansion, Marangoni flux becomes negligible to leading order, and the vertical growth of the neck height is driven primarily by capillary effects. In this regime, the governing equations simplify to

$$\partial_t h - \nabla \cdot \left(\frac{h^3}{3} \nabla p \right) = 0, \tag{3.3}$$

$$p + \nabla \cdot \left(\nabla h - \beta \frac{\Gamma_0}{2} \left(1 - \operatorname{erf} \left(\frac{Pe^{1/2} x}{2t^{1/2}} \right) \right) \nabla h \right) = 0. \tag{3.4}$$

Equation (3.4) uses the analytical expression for $\Gamma(x,t)$ obtained earlier. Although the Marangoni effect formally appears in the pressure expression, its influence on height evolution is subdominant at early times.

Previous studies (Hernández-Sánchez et al., 2012; Kaneelil et al., 2022) demonstrated emergence of self-similarity in early-stage drop coalescence, where dynamics are governed by a single evolving length scale. In this regime, scaled bridge profiles collapse onto a universal curve. Motivated by these findings, we seek a similarity solution to our reduced system of equations (3.3) and (3.4).

Consistent with our numerical observations, we postulate a similarity form in which the film height grows linearly in time:

$$h(x,t) = vt\,\mathcal{H}(\varsigma), \qquad \varsigma = \frac{x}{vt}, \tag{3.5}$$

where v is a constant to be determined, and $\mathcal{H}(\varsigma)$ represents the similarity profile of the liquid bridge.

To proceed analytically, we expand the error function in the pressure term using a

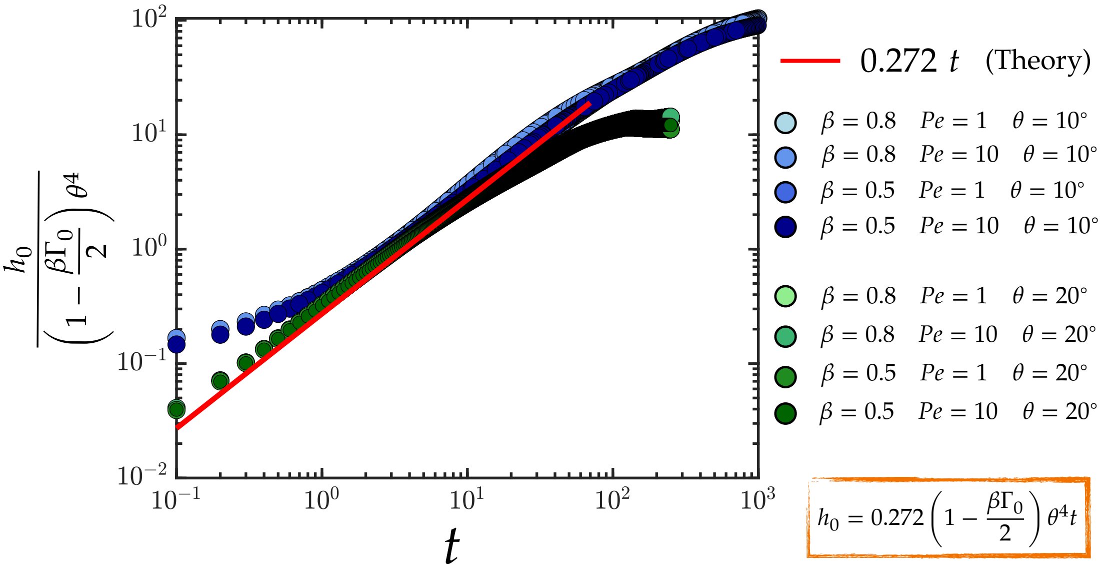

Figure 3.5: *Compensated neck height evolution showing collapse of all data onto a single master curve when plotted as* $h_0/\left[(1-\beta\Gamma_0/2)\,\theta^4\right]$ *versus time* t. *The red line corresponds to the theoretical prediction* $h_0 = 0.272\,t$, *derived from similarity analysis with no adjustable parameters.*

Taylor series:

$$\mathrm{erf}(z) = \frac{2}{\sqrt{\pi}}\left(z - \frac{z^3}{3} + \mathcal{O}(z^5)\right),$$

and retain only the leading-order term. Substituting the similarity ansatz (3.5) into equations (3.3) and (3.4) yields an ordinary differential equation (ODE) for the similarity profile $\mathcal{H}(\varsigma)$:

$$\mathcal{H} - \varsigma\mathcal{H}' + \frac{1-\beta\Gamma_0/2}{v}\left(\mathcal{H}^3\mathcal{H}'''\right)' = 0.$$

To solve the similarity equation, we recognize that it is a fourth-order ODE containing a single unknown parameter v. Therefore, a total of five boundary conditions are required to obtain a unique solution.

Solving this fourth-order ODE requires five boundary conditions. At the bridge center ($\varsigma = 0$), we assume interface symmetry, justified by absence of Marangoni fluxes in the leading-order approximation:

$$\mathcal{H}(0) = 1, \quad \mathcal{H}'(0) = 0, \quad \mathcal{H}'''(0) = 0.$$

Far from the neck ($\varsigma \to \infty$), the profile is expected to match the outer solution corresponding to a linear slope determined by the contact angle θ:

$$\mathcal{H}''(\infty) = 0, \quad \mathcal{H}'(\infty) = 1.$$

This boundary value problem uniquely determines both the similarity profile $\mathcal{H}(\varsigma)$ and the dimensionless coalescence velocity v. Solving numerically using a shooting method yields

$$v = 0.272\left(1 - \frac{\beta\Gamma_0}{2}\right),$$

demonstrating that the surfactant effect enters through a linear reduction in coalescence rate. The resulting profile $\mathcal{H}(\varsigma)$ captures the self-similar shape of the neck during the early-time dynamics.

From the similarity solution, the neck height is predicted to evolve linearly with time as:

$$h_0 = vt = 0.272\left(1 - \frac{\beta\Gamma_0}{2}\right)t.$$

Incorporating dependence on contact angle θ from the original non-dimensional formulation gives the corrected scaling law:

$$h_0 = vt = 0.272\left(1 - \frac{\beta\Gamma_0}{2}\right)\theta^4 t.$$

Figure 3.5 presents the compensated neck height $h_0/\left[\left(1 - \frac{\beta\Gamma_0}{2}\right)\theta^4\right]$ versus time. After rescaling, all data collapse onto a single master curve, validating the theoretical prediction. The red line, corresponding to $0.272t$, provides excellent prediction without adjustable parameters.

Notably, the resulting expression for the neck height in the surfactant-laden case with low Pe matches the analytical result derived by Hernández-Sánchez et al. (2012), but with a multiplicative correction factor $\left(1 - \frac{\beta\Gamma_0}{2}\right)$. In the low Péclet number regime, surfactants primarily reduce effective surface tension. Marangoni stresses, while present, do not significantly contribute to early-time neck growth.

Highlight

Height of the neck for low Pe, $h_0 = 0.272\left(1 - \frac{\beta\Gamma_0}{2}\right)\theta^4 t$

3.2.3 Horizontal Movement

We examine horizontal neck motion by tracking the position of the liquid bridge minimum, $x_0(t)$. At early times, interfacial surfactant concentration is asymmetric: the left drop contains surfactant, while the right drop does not. This creates a surface tension gradient, with the left drop having lower surface tension. The resulting gradient induces Marangoni stress directed from low to high surface tension, from left to right.

The tangential Marangoni stress is

$$\nabla_s\gamma = -\beta\nabla_s\Gamma \approx -\beta\frac{\partial\Gamma}{\partial x},$$

where the surface gradient operator ∇_s is approximated by the planar derivative ∂_x,

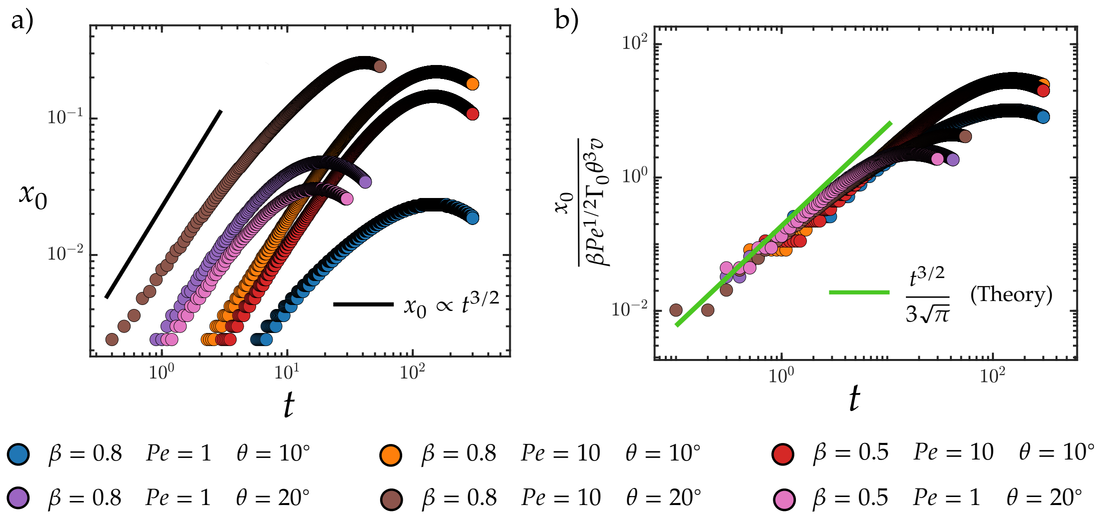

Figure 3.6: *(a) Evolution of the neck position x_0 as a function of time for various combinations of β, Pe, and θ. At early times, the data follow a clear $x_0 \propto t^{3/2}$ power law (black line), (b) compensated plot of x_0 scaled by the theoretical prediction $\frac{\beta Pe^{1/2}\Gamma_0 v}{3\sqrt{\pi}} t^{3/2}$. The data collapse onto the theoretical line (green), confirming the early-time scaling without fitting parameters.*

valid in the lubrication limit (see Section 2.2). This Marangoni-driven flow promotes rightward neck motion.

Simultaneously, spatial variation in surfactant concentration leads to differing surface tensions on the left and right bridge sides, γ_1 and γ_2 respectively. These variations create asymmetric Laplace pressure contributions driving flow toward the neck. Since the right drop has higher surface tension $(\gamma_2 > \gamma_1)$, it contributes larger Laplace pressure gradient toward the neck. This pressure imbalance pushes fluid leftward.

The net Laplace pressure driving force across the neck due to surface tension difference is

$$\Delta p_{\text{Laplace}} = (\gamma_2 - \gamma_1)\nabla^2 h.$$

While Marangoni forces drive the neck rightward, differential Laplace pressures oppose this motion. Since the surfactant concentration gradient is initially very steep near the neck,

$$\left.\frac{\partial \Gamma}{\partial x}\right|_{x=0} \to \infty,$$

the tangential Marangoni force dominates early-time dynamics. Figure 3.6a) shows the neck minimum position $x_0(t)$ exhibits power-law scaling with time, following $x_0 \propto t^{3/2}$, a direct consequence of Marangoni-driven flow toward higher surface tension.

As time progresses, surfactant diffusion smooths out the concentration gradient, leading to a gradual decay in Marangoni stresses. Simultaneously, the bridge continues to evolve asymmetrically, shifting toward the right and creating an imbalance in Laplace pressure across the neck. While the Marangoni force diminishes, the Laplace pressure – now driven by interfacial asymmetry – becomes the dominant mechanism.

At later times, this competition arrests forward motion. The neck position $x_0(t)$

flattens and reaches a maximum before receding. As shown in Figure 3.6a), this reversal marks when the surfactant profile has become uniform and the only remaining driving force is pressure imbalance from geometrical asymmetry, pushing the neck leftward.

To further understand early-time horizontal motion dynamics, we examine tangential surface velocity at the neck. According to lubrication theory (Oron et al., 1997), surface velocity along the interface is:

$$u_s = -\frac{\partial p}{\partial x}\frac{h_0^2}{2} - \beta\frac{\partial \Gamma}{\partial x}h_0.$$

The first term represents contribution from Laplace pressure gradients, while the second arises from surface tension gradients (Marangoni stresses). Under the low Péclet number regime, asymptotic analysis reveals the pressure gradient term is subdominant. Therefore, surface velocity is primarily governed by the Marangoni contribution:

$$\begin{aligned} u_s &= -\beta\frac{\partial \Gamma}{\partial x}h_0 \\ &= \frac{\beta Pe^{1/2}\Gamma_0}{2\sqrt{\pi}t^{1/2}}\, h_0 \exp\left(-\frac{Pe\, x^2}{4t}\right). \end{aligned}$$

To derive an analytical expression for neck displacement $x_0(t)$ at early times, we expand the exponential using Taylor series:

$$\exp(z) = 1 + z + \frac{z^2}{2} + O(z^3).$$

Substituting $h_0 = vt$ into the Marangoni-dominated velocity expression and retaining leading-order terms gives:

$$\begin{aligned} u_s &= \frac{\beta Pe^{1/2}\Gamma_0}{2\sqrt{\pi}t^{1/2}} h_0 \left(1 - \frac{Pe\, x^2}{4t} + O(Pe^2)\right) \\ &= \frac{\beta Pe^{1/2}\Gamma_0 v}{2\sqrt{\pi}} t^{1/2}. \end{aligned}$$

Integrating this surface velocity in time gives early-time neck displacement:

$$x_0(t) = \int_0^t u_s(\tau)\, d\tau = \frac{\beta Pe^{1/2}\Gamma_0 v}{3\sqrt{\pi}} t^{3/2}.$$

This confirms the power-law behavior $x_0 \propto t^{3/2}$ observed in simulations (Figure 3.6a). Figure 3.6b) shows a compensated plot of x_0 with theoretical prediction

$$\frac{t^{3/2}}{3\sqrt{\pi}}$$

as reference. Agreement between theory and numerics is excellent without adjustable parameters.

Highlight

`Moving front of the neck for low` Pe, $x_0 = \frac{\beta Pe^{1/2}\Gamma_0 v}{3\sqrt{\pi}} t^{3/2}$

3.3 Summary

This chapter examined coalescence dynamics of surfactant-laden viscous drops in the low Péclet number limit. Surfactant diffusion rapidly homogenizes surface tension, suppressing Marangoni effects at late times. Neck height evolves as

$$h_0 = \left(1 - \frac{\beta\Gamma_0}{2}\right)\theta^4 t,$$

consistent with classical viscous coalescence but corrected for reduced surface tension. At early times, Marangoni-driven flow displaces the neck horizontally as $x_0 \propto t^{3/2}$ before reversing due to asymmetric Laplace pressure. Analytical predictions matched simulations without fitting parameters.

4

Intermezzo: Maximum Horizontal Movement

The horizontal displacement dynamics introduced in Section 3.2.3 reveal a turning point after surfactant redistribution completes. In this chapter, we focus on this turning behavior by investigating the point of maximum neck displacement, which occurs when the surfactant gradient vanishes and only geometric asymmetry remains.

Figure 4.1 shows the interface and velocity field evolution for $\beta = 0.9$, $\theta = 20°$, and $Pe = 10$. The top panels display surfactant concentration Γ with velocity vectors, while the bottom panels highlight the dominant flow mechanisms.

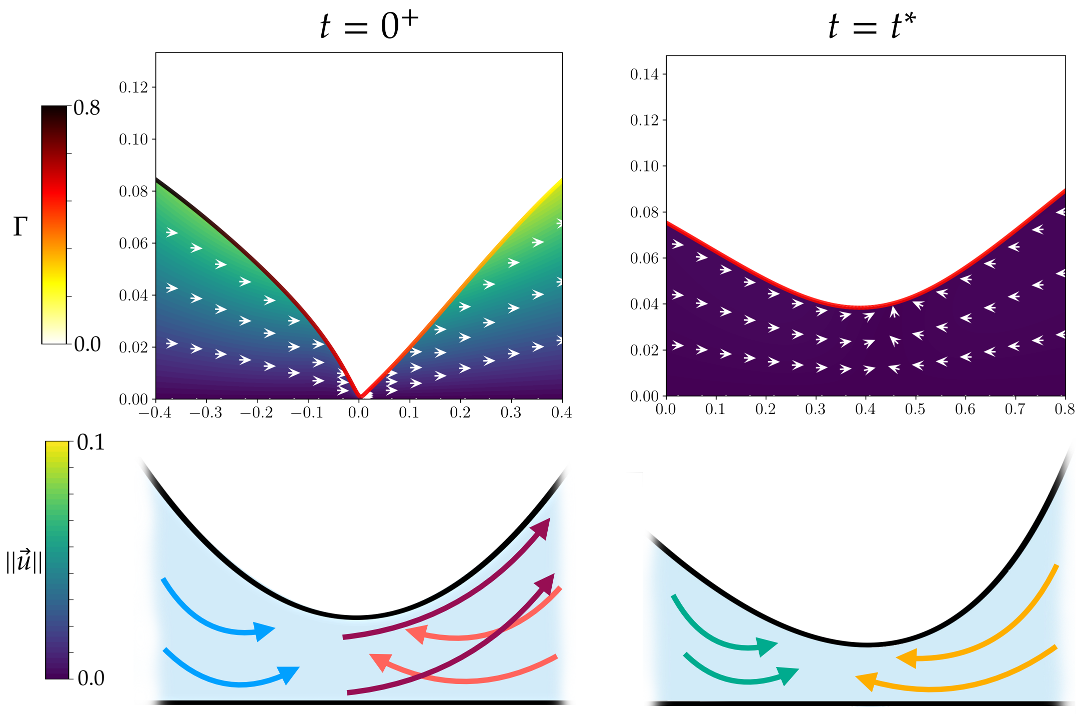

Figure 4.1: *Flow field and surfactant concentration evolution near the neck at early and intermediate times for* $\beta = 0.9$, $\theta = 20°$, *and* $Pe = 10$. (***Top***) *Velocity magnitude and vector fields overlaid on surfactant concentration at* $t = 0^+$ *and at the turning point* $t = t^*$. (***Bottom***) *Schematic representations of the dominant forces.*

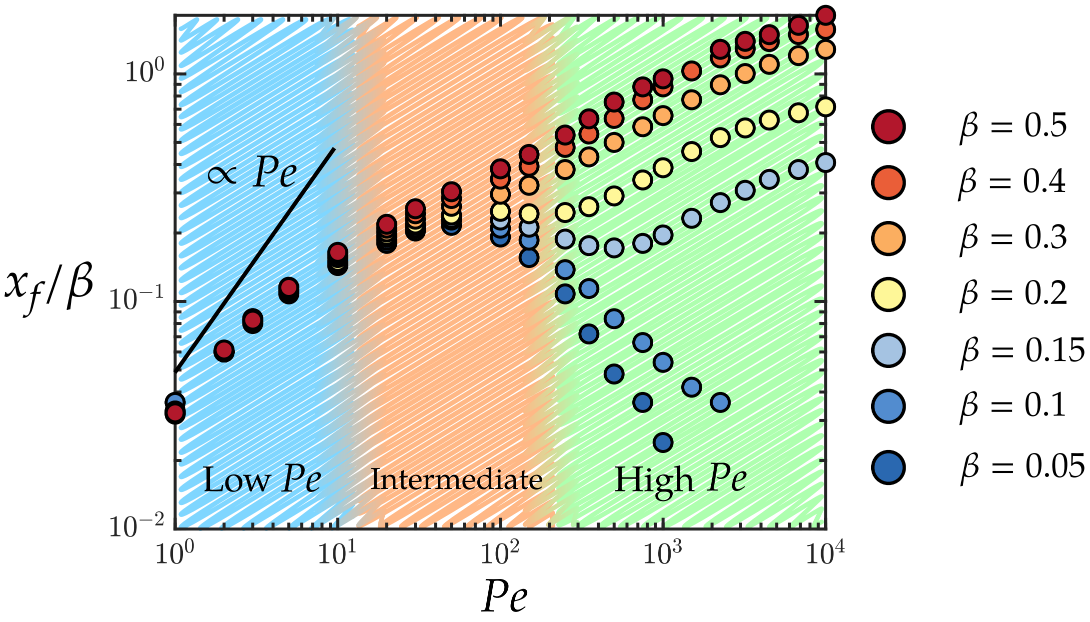

Figure 4.2: *Scaling of maximum horizontal displacement* x_f *normalized by* β *as a function of Péclet number* Pe*, shown for a range of surfactant strengths* β*.*

At $t \rightarrow 0^+$, the large surfactant gradient $\partial\Gamma/\partial x \gg 1$ generates strong Marangoni stresses (→) directed rightward. Additionally, surface tension asymmetry creates Laplace pressure differences: the left drop with lower surface tension contributes less pressure (→) than the right drop (←). The nearly symmetric drops at this instant generate asymmetry solely from surface tension differences.

At a later time $t = t^*$, complete surfactant diffusion produces uniform concentration near the neck, eliminating Marangoni forces. However, prior bridge movement creates geometric asymmetry that drives asymmetric Laplace pressure distribution. The neck reaches its maximum horizontal position x_f before reversing due to this pressure imbalance.

After reaching maximum displacement, the dynamics resemble asymmetric coalescence described by Hernández-Sánchez et al. (2012). In the next section, we examine how x_f scales with the Péclet number.

4.1 Scaling Laws in the Low Pe Regime

The maximum horizontal displacement x_f increases monotonically with Pe in the low-Pe regime (Figure 4.2). Larger Pe extends the diffusive timescale $t_d = Pe{\cdot}t_c$, sustaining Marangoni stresses longer and increasing rightward neck motion.

To further highlight this scaling, we plot x_f/β versus Pe. The collapse of data in the low Pe regime indicates that the surfactant strength enters linearly into the Marangoni force.

To understand this behavior physically, we examine the vertical velocity scale of the bridge meniscus which can be approximated using the characteristic capillary velocity:

$$\mathcal{V}_{\perp} \sim \frac{\gamma_0}{\mu},$$

In the horizontal direction, the flow is primarily driven by Marangoni stresses, which give rise to a characteristic interfacial velocity scale, denoted $\mathcal{V}_{\parallel}$. This velocity scale can be estimated by the stress-free boundary condition at the interface, as described in Berg (2009), Eshima et al. (2024), and Temprano-Coleto and Stone (2024):

$$\mu\frac{\partial u}{\partial z} = -a\frac{\partial \Gamma}{\partial x}$$
$$\Rightarrow \mathcal{V}_{\parallel} \sim \frac{a\Gamma_\infty}{\mu}.$$

We have previously seen that the diffusive timescale as $t_d = \frac{L^2}{D_s}$. Using this, the maximum horizontal displacement of the neck can be estimated as:

$$x_f^* \sim \mathcal{V}_{\parallel} \cdot t_d \sim \frac{a\Gamma_\infty}{\mu} \cdot \frac{L^2}{D_s}.$$

Normalizing by the drop radius L, we obtain:

$$x_f \sim \beta Pe.$$

This scaling confirms that the horizontal displacement x_f grows linearly with the Marangoni number $Ma = \beta Pe$ (the product of the surfactant strength number β and Péclet number Pe), consistent with the numerical trend in Figure 4.2.

Highlight

`Maximum horizontal movement of the neck for low` Pe, $x_f \sim \beta Pe$

4.2 Non-Monotonic Behaviour

Figure 4.2 reveals non-monotonic behavior in x_f versus Pe. While x_f increases with Pe at low values due to prolonged Marangoni activity, the trend reverses beyond a critical point.

Interestingly, this non-monotonicity emerges only above a critical surfactant strength number β_c. For $\theta = 20^\circ$, $\beta_c \approx 0.15$. Above this threshold, x_f grows monotonically with Pe; below it, x_f peaks then decreases with further increases in Pe.

In the limit $Pe \to \infty$ where diffusion vanishes and the surfactant field remains frozen, the system exhibits a sharp transition between coalescence ($x_f \ll 1$) and non-coalescent motion (finite x_f) depending on whether $\beta < \beta_c$ or $\beta > \beta_c$. This transition parallels observations in binary drops by Karpitschka and Riegler (2014), where

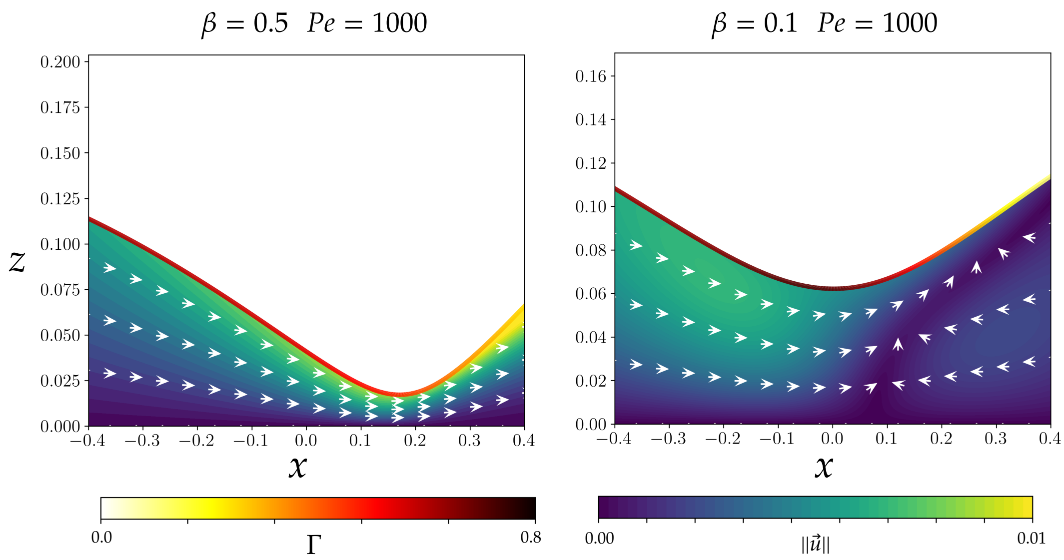

Figure 4.3: *Comparison of velocity fields and surfactant concentration profiles at $t = 30$ for two cases with $Pe = 1000$ and $\theta = 20°$. (**Left**) For $\beta = 0.5 > \beta_c$, the neck has significantly displaced rightward, consistent with strong sustained Marangoni forcing. (**Right**) For $\beta = 0.1 < \beta_c$, despite similar rightward velocity fields, the neck remains near $x = 0$.*

Marangoni stresses drive abrupt coalescence behavior changes. The binary drop case, lacking diffusive transport, represents the $Pe \to \infty$ limit of our system.

Figure 4.3 further exemplify this bifurcation-type dynamics by comparing the velocity vectors and surfactant concentration for $\beta = 0.5 > \beta_c$ and $\beta = 0.1 < \beta_c$ at $Pe = 1000$, $\theta = 20°$, and $t = 30$. Both cases show predominantly rightward flow from surface tension gradients. For $\beta = 0.5$, the neck moves with the flow, showing significant horizontal displacement. For $\beta = 0.1$, the neck remains near $x = 0$ despite similar flow directions.

In the high-Pe regime, Marangoni forces displace the neck only when $\beta > \beta_c$. The underlying mechanisms are examined in the next chapter.

4.3 Summary

We analyzed the maximum horizontal displacement x_f of the neck. At low Pe, x_f scales as βPe, driven by sustained Marangoni stresses. Non-monotonic behavior in x_f emerges beyond a critical surfactant strength β_c, marking a sharp transition between coalescence and non-coalescence. This mirrors binary drop observations, corresponding to the $Pe \to \infty$ limit. Flow visualizations confirm that neck motion in the high-Pe regime requires $\beta > \beta_c$.

5

DROP NON-COALESCENCE: HIGH Pe LIMIT

The previous chapter revealed non-monotonic behavior of neck displacement x_f with Péclet number Pe. This chapter examines the physical origins by comparing two representative cases:

- Case (a): $\beta = 0.1$, $Pe = 1000$, $\theta = 20°$
- Case (b): $\beta = 0.5$, $Pe = 1000$, $\theta = 20°$

Both configurations lie in the high-Pe regime (Figure 4.2). However, Case (a) shows decreasing x_f with increasing Pe, while Case (b) shows the opposite. This comparison reveals the mechanisms driving non-monotonic neck motion.

5.1 Escape from Non-Coalescence

In the low-Pe regime, diffusion dominates convection. Surfactants uniformly reduce bridge surface tension by $\left(1 - \frac{\beta\Gamma_0}{2}\right)$ (Section 3.2.2), yielding symmetric capillary-driven evolution.

We now consider the high-Pe case: $\beta = 0.5$, $Pe = 1000$, $\theta = 20°$ (Figure 4.2). The surfactant concentration (Figure 5.1, middle panel) remains nearly uniform for $x < 0$, exhibits a steep gradient in $0 < x < 0.5$, and drops to zero beyond.

This localized gradient region drives Marangoni transport. To analyze the flow response here, we examine the surface velocity u_s, decomposed into contributions from Laplace pressure gradients and Marangoni stresses as

$$u_s = \underbrace{-\frac{\partial p}{\partial x}\frac{h^2}{2}}_{\text{Laplace}} + \overbrace{-\beta\frac{\partial \Gamma}{\partial x}h}^{\text{Marangoni}} \, .$$

At low Pe, as shown through the perturbation analysis, the contribution of the Laplace term in the surface velocity u_s is negligible compared to the Marangoni term. However, in the high-Pe regime, both components contribute at the same order of

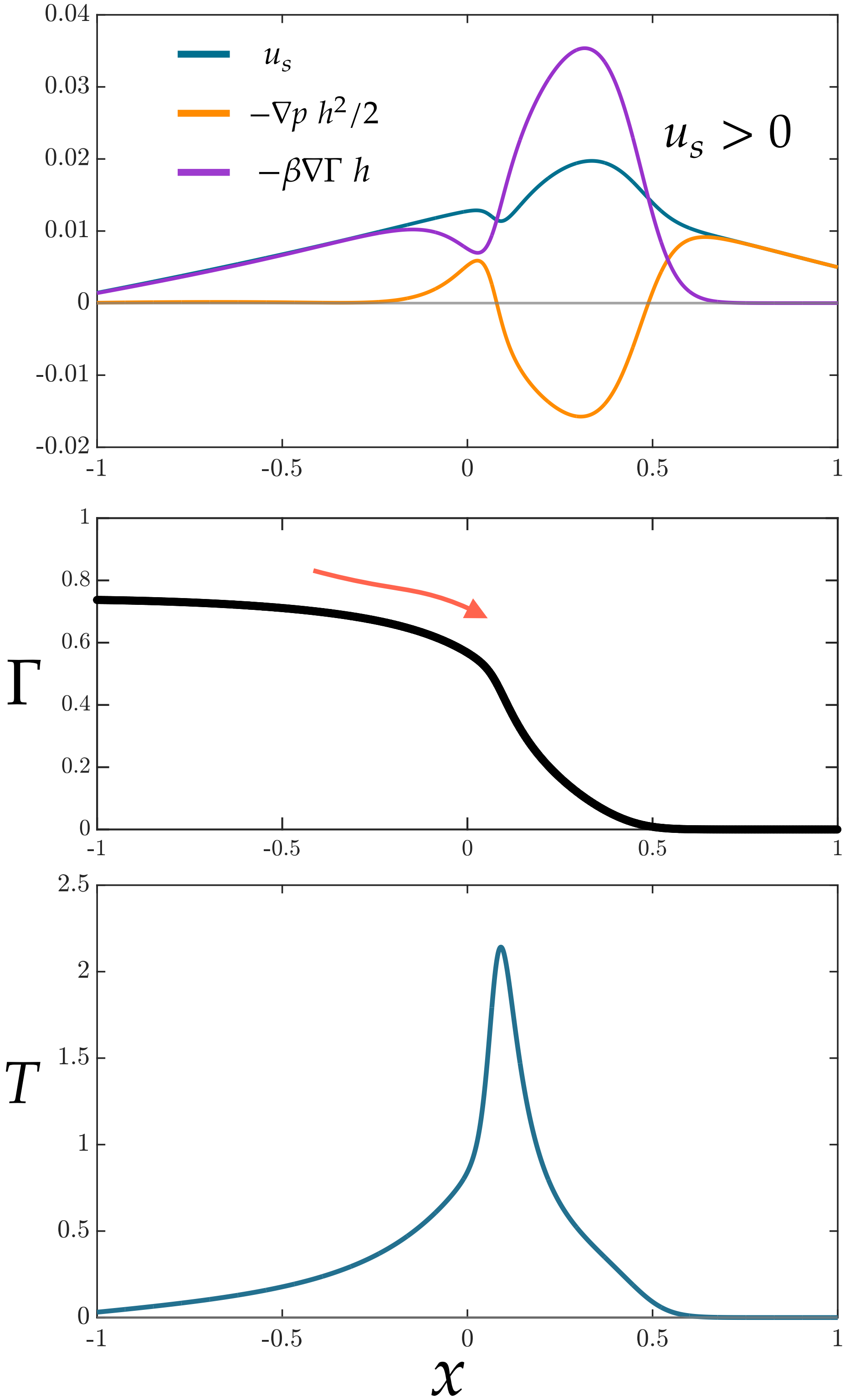

Figure 5.1: *Decomposition of surface velocity and resulting Marangoni stress for* $\beta = 0.5$, $Pe = 1000$, *and* $\theta = 20°$. (***Top***) *Tangential velocity* u_s *(blue), Laplace contribution* $-\nabla p\, h^2/2$ *(orange), and Marangoni term* $-\beta\nabla\Gamma\, h$ *(purple).* (***Middle***) *Monotonic surfactant concentration profile* $\Gamma(x)$ *resulting from continuous rightward convection.* (***Bottom***) *Marangoni stress* $T(x)$ *shows a single pronounced peak, leading to unidirectional rightward motion of the neck.*

magnitude. The Laplace term is negative (opposing flow), while the Marangoni term is positive (Figure 5.1).

For the case $\beta = 0.5$, $Pe = 1000$, Marangoni stress maintains $u_s > 0$ everywhere, driving continuous rightward surfactant convection. The concentration profile becomes monotonic (Figure 5.1, middle panel), decreasing steadily from left to right.

The Marangoni stress driving this behavior is:

$$T = -\frac{\beta}{1-\Gamma}\frac{\partial \Gamma}{\partial x}.$$

Here, we stress that the term $1-\Gamma$ accounts for surfactant coverage. Under lubrication approximation, the surface gradient reduces to $\partial\Gamma/\partial x$. The stress exhibits a single peak near the surfactant front (Figure 5.1, bottom panel), driving persistent rightward neck motion.

In contrast to the above scenario, for $\beta = 0.1$ (Figure 5.2), the weaker Marangoni contribution $-\beta\nabla\Gamma h$ cannot overcome the negative Laplace pressure term. The net surface velocity becomes negative near $x \approx 0.2$. Negative u_s drives leftward surfactant advection. While surfactants convect rightward for $x < 0$, they move leftward for $x > 0.2$. This bidirectional transport accumulates surfactants in the intermediate zone, creating a non-monotonic profile with a local peak (Figure 5.2, middle panel).

This non-monotonicity generates Marangoni stress with two opposing peaks (Figure 5.2, bottom panel). The net driving force depends on their imbalance, resulting in weakened, symmetric Marangoni response that slows horizontal neck displacement. As Pe increases for fixed $\beta = 0.1$, the negative peak strengthens, further reducing x_f. This explains the non-monotonic behavior for $\beta < \beta_c$ in Figure 4.2.

The negative Marangoni stress peak magnitude increases with Pe due to intensified leftward advection in the $x > 0.2$ region. This sharpens surfactant accumulation and concentration gradients. The mechanism driving consistent growth of negative u_s with Pe at fixed $\beta < \beta_c$ requires further investigation.

5.1.1 Vorticity Generation at the Free Surface

Marangoni stresses induce flow reversal on the right neck side within a thin boundary layer. These stresses strengthen over time, causing flow separation and vortex ring formation near the interface.

This naturally raises the question: can the escape from non-coalescence be understood as a coherent physical process governed by a common mechanism? To explore this idea, it is useful to recognize that the formation of a boundary layer within an otherwise potential flow is closely associated with the generation of vorticity $\omega = \nabla \times \vec{u}$. The role of boundary layers in introducing vorticity into free-surface flows has been widely examined in the literature (Rood, 1994; Lundgren and Koumoutsakos, 1999).

Figure 5.3 shows strong vorticity accumulation for $\beta = 0.1$ but none for $\beta = 0.5$. This vorticity flux arises from negative Marangoni stress, injecting vorticity into the

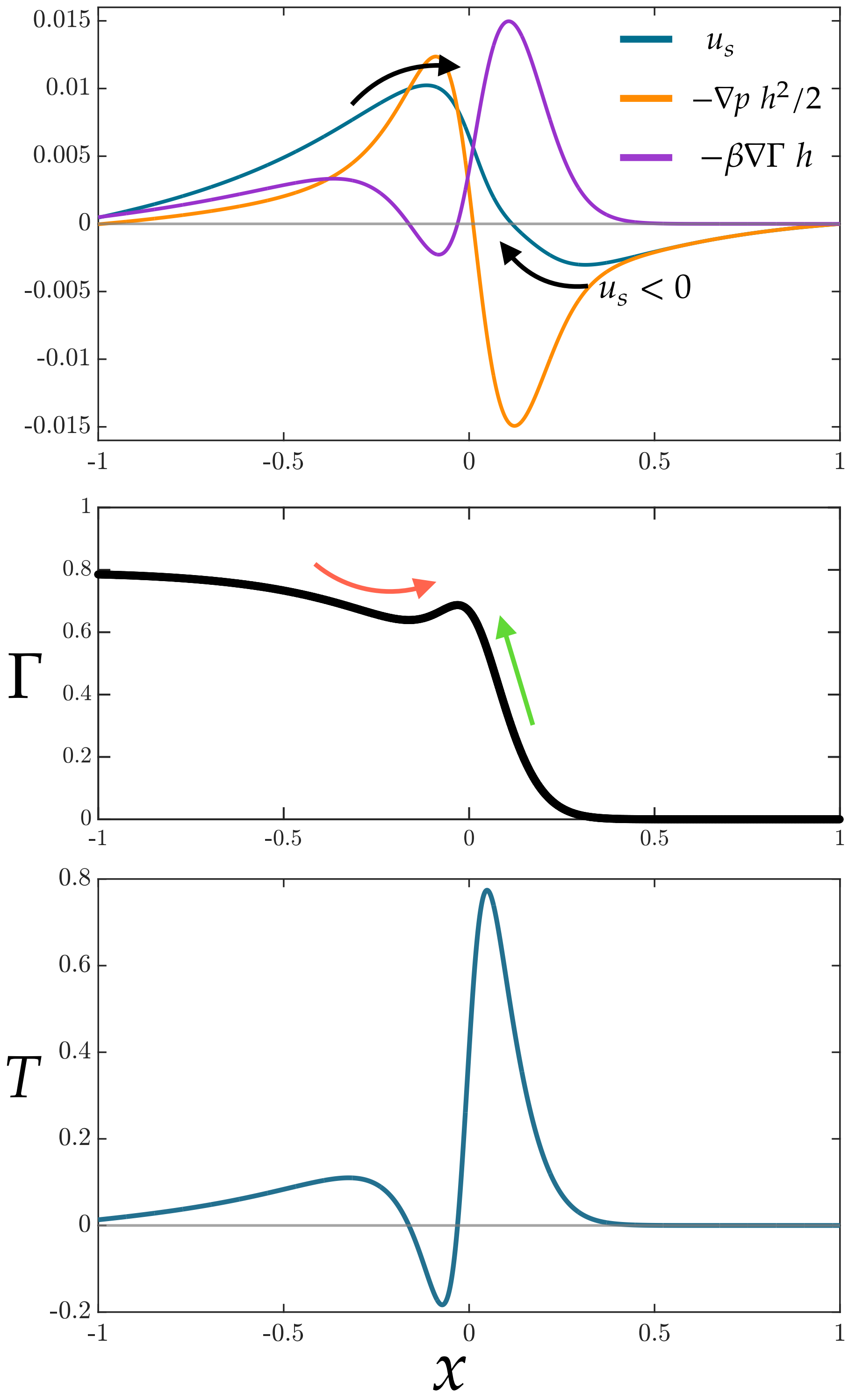

Figure 5.2: *Surface velocity decomposition and surfactant dynamics for* $\beta = 0.1$, $Pe = 1000$, *and* $\theta = 20°$. (***Top***) *The Laplace contribution (orange) dominates over the weaker Marangoni term (purple), resulting in a negative surface velocity* u_s *(blue) near* $x \approx 0.2$, *leading to leftward advection in that region.* (***Middle***) *Surfactant concentration* $\Gamma(x)$ *exhibits a non-monotonic peak due to opposing transport directions.* (***Bottom***) *Marangoni stress* $T(x)$ *displays two peaks of opposite sign, weakening net interfacial driving and reducing neck displacement.*

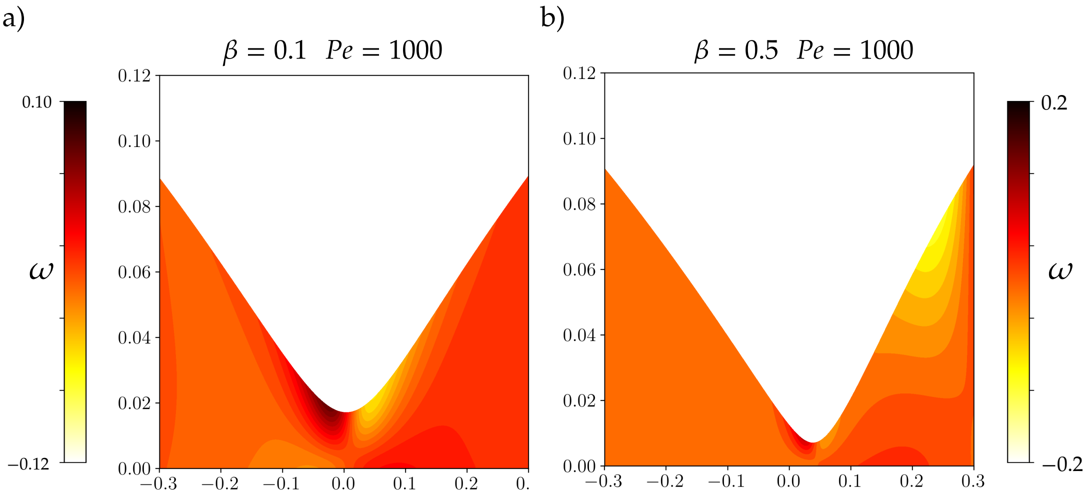

Figure 5.3: *Vorticity field ω near the neck region for two cases at $Pe = 1000$ and $\theta = 20°$. (**a**) For $\beta = 0.1$, strong vorticity generation is observed near the neck. (**b**) For $\beta = 0.5$, vorticity generation is minimal near the neck, and flow separation is not observed.*

boundary layer. The presence or absence of this vorticity accumulation acts as a kind of *fingerprint check* for whether a drop can escape non-coalescence. Sufficient vorticity generation enables backflow within the boundary layer to refill the neck, preventing non-coalescence by linking localized interfacial stresses to macroscopic fluid rearrangement.

Interestingly, Kamat et al. (2020) reported a similar phenomenon filament pinch-off. Highly stretched, low-viscosity filaments exceeding critical aspect ratio undergo localized end-pinching, creating daughter droplet cascades. However, the addition of surfactants suppress this behavior, allowing escape from end-pinching.

The common feature underlying these escape phenomena is the generation of vorticity at curved, surfactant-laden interfaces. Hoepffner and Paré (2013) showed this mechanism modifies classical vorticity balance within deforming volume $V(t)$ enclosed by free surface $S(t)$:

$$\frac{D}{Dt}\int_{V(t)} \omega\, dV = \int_{V(t)} \omega\cdot\nabla\vec{u}\, dV + 2\,Oh\int_{S(t)} \mathbf{e}_\theta \mathbf{n}\cdot\nabla\left(\frac{\partial u_n}{\partial s} - \kappa_t u_t\right) dS + \int_{S(t)} \mathbf{e}_\theta \mathbf{n}\cdot\nabla(-T)\, dS.$$

Here $Oh = \mu/\sqrt{\rho L \gamma}$ is the Ohnesorge number, $\mathbf{e}_\theta$ the azimuthal unit vector, and κ_t the principal curvature. The final term introduces surface-based vorticity generation from Marangoni stress, confirming large negative T drives interfacial vorticity accumulation enabling escape from non-coalescence.

Highlight

Below β_c, negative Marangoni stresses generate vorticity that arrests the horizontal motion of the neck even at $Pe \longrightarrow \infty$.

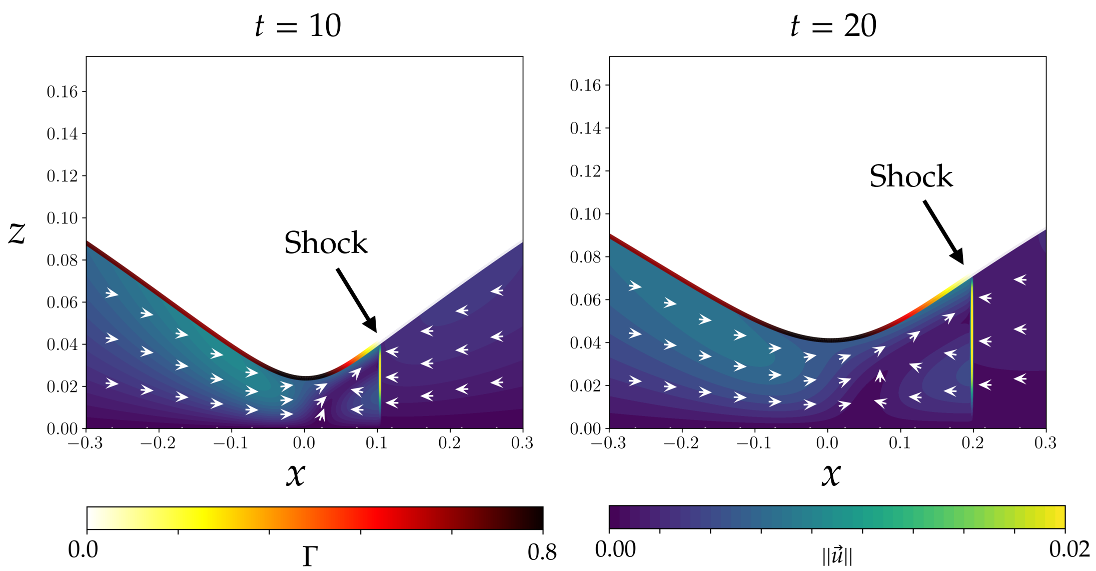

Figure 5.4: *Formation and evolution of a kinematic shock in the high-Pe limit for* $\beta = 0.1$*,* $Pe = 10^6$*, and* $\theta = 20°$*. (**Left**) At* $t = 10$*, a sharp surfactant front forms near* $x \approx 0.1$*, accompanied by a discontinuity in the velocity magnitude* $\|\vec{u}\|$*. (**Right**) By* $t = 20$*, this shock has propagated further to the right, maintaining a steep velocity gradient and a discontinuous drop in surfactant concentration.*

5.2 Shock Solutions at High Pe

We now investigate the system behavior in the asymptotic high Péclet number limit. Figure 5.4 shows bridge meniscus evolution for $\beta = 0.1$, $Pe = 10^6$, $\theta = 20°$. Since $\beta < \beta_c$, the bridge moves vertically upward rather than horizontally. However, a striking new phenomenon emerges: a kinematic shock forms and propagates rightward along the free surface.

The shock appears as a flow field discontinuity in both panels of Figure 5.4. Velocity magnitude $|\vec{u}|$ jumps sharply at the shock front, implying a corresponding pressure jump. The shock coincides with where surfactant concentration Γ drops to zero.

As $Pe \to \infty$, negligible diffusion yields purely convective transport, forming a sharp concentration front separating surfactant-laden and surfactant-free regions. At front position $x = x_s(t)$: ahead $(x = x_s^+)$, $\Gamma = \nabla\Gamma = 0$ and $u_s(x_s^+, t) = u_s^+ = 0$; behind $(x = x_s^-)$, finite concentration yields nonzero velocity $u_s(x_s^-, t) = u_s^-$. This discontinuity characterizes nonlinear kinematic wave propagation (Whitham, 1974; Gaver and Grotberg, 1990). This shock-like behavior is a distinct feature of the high-Pe regime, where sharp convective fronts form in the absence of diffusion.

5.3 $1/Pe = 0$ Limit

Examining $Pe \to \infty$ by neglecting diffusion reduces the surfactant equation to:

$$\partial_t \Gamma + \nabla_s \cdot (\Gamma u_s) = 0.$$

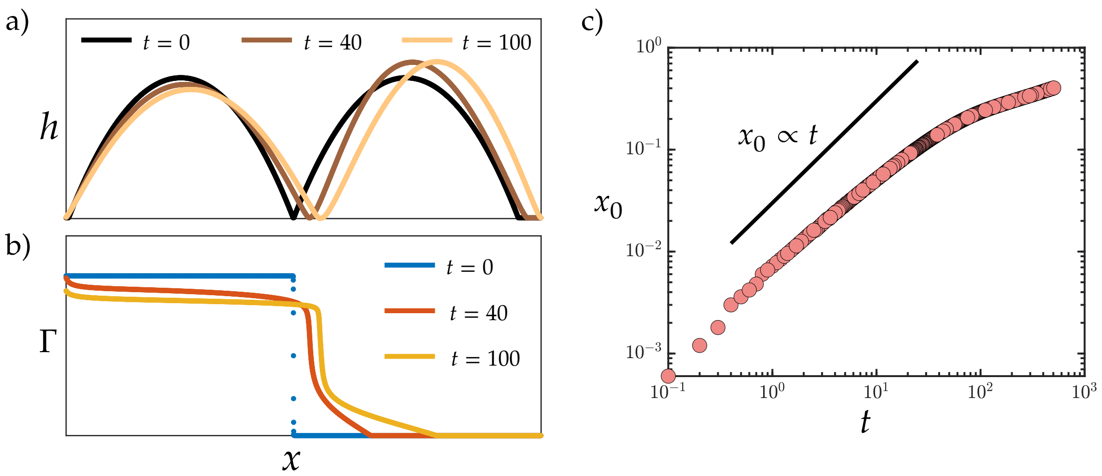

Figure 5.5: *Dynamics of the surfactant-laden drops in the convection-dominated limit* $(1/Pe = 0)$ *with* $\beta = 0.1$ *and* $\theta = 20°$. (***a***) *Height profiles* $h(x,t)$ *at different times showing negligible vertical motion of the neck.* (***b***) *Surfactant concentration* $\Gamma(x,t)$ *remains sharply divided with a steep front that advects over time.* (***c***) *Temporal evolution of the horizontal neck position* $x_0(t)$ *initially follows a linear law* $(x_0 \propto t)$.

Figure 5.5 shows the system evolution under this condition. Panel (a) presents interface height profiles; panel (b) shows surfactant concentration evolution. The neck height remains nearly stationary, resembling Karpitschka and Riegler (2012)'s stable twin-drop configuration.

The lack of neck evolution removes one of the characteristic length scales of the problem, leaving only the horizontal displacement x_0, which initially scales linearly with time as $x_0 \propto t$ (Figure 5.5c). At later times, however, x_0 deviates from this linear behavior as the neck flattens and a steady thin film region emerges between the drops.

Without diffusion, the surfactant profile remains sharply segregated: constant Γ_0 on the left, zero on the right. This abrupt transition persists through advection alone. Even in the $1/Pe = 0$ limit, a kinematic shock is observed at the surfactant front. One compelling explanation for the existence of such a shock comes from a mathematical perspective. Thess et al. (1995) derived a one-dimensional formulation for Stokes flow with surfactant transport using Fourier transforms, yielding:

$$u_s(x,t) = \frac{\beta}{2\pi}\,\text{p.v.}\int_{-\infty}^{\infty} \frac{\Gamma(x',t)}{x-x'}\,dx' = \frac{\beta}{2}H[\Gamma],$$

where p.v. denotes the Cauchy principal value and $H[\cdot]$ represents the Hilbert transform operator.

Substituting into the surfactant transport equation yields a closed nonlinear conservation law:

$$\frac{\partial \Gamma}{\partial t} + \frac{\beta}{2}\frac{\partial}{\partial x}\left(H[\Gamma]\cdot\Gamma\right) = 0, \quad \Gamma(x,t=0) = \Gamma_0(x).$$

In the context of Marangoni-driven flows, Crowdy (2021) recently presented a complex-variable formulation introducing a complex-dependent variable ψ, given by

$$\psi = u_s + i\Gamma = H[\Gamma] + i\Gamma,$$

satisfying

$$\frac{\partial \psi}{\partial t} + \frac{\beta \psi}{2}\frac{\partial \psi}{\partial x} = 0, \qquad \psi(x, t = 0) = \psi_0(x) = H[\Gamma_0(x)] + i\Gamma_0(x),$$

where $\psi(z, t)$ must be a lower-analytic complex function in the complex variable $z = x + iy$.

This complex inviscid Burgers equation develops shock discontinuities from smooth initial conditions. Shocks in ψ create sharp surfactant fronts and surface velocity discontinuities. Our lubrication formulation, approximating Stokes equations, may admit similar complex-analytic structures and shock solutions.

5.3.1 Similarity Transform

We explore self-similar solutions at infinite Péclet number by adopting a similarity ansatz that assumes the height and surfactant fields as:

$$h(x, t) = h_0(t)\, H(\varsigma), \qquad \Gamma(x, t) = \Gamma_0(t)\, \Phi(\varsigma),$$

where the similarity variable ς is defined in a co-moving frame centered at the neck and scaled by the evolving horizontal extent $\delta(t)$:

$$\varsigma = \frac{x - x_0(t)}{\delta(t)}.$$

We start from the evolution equation for the film height:

$$\partial_t h + \nabla \cdot \left(-\frac{h^3}{3}\nabla p - \beta \frac{h^2}{2}\nabla\Gamma \right) = 0.$$

Using the chain rule, the temporal derivative becomes:

$$\partial_t h = \dot{h}_0(t)\, H(\varsigma) - h_0(t)\, H'(\varsigma) \left(\frac{\dot{x}_0(t)}{\delta(t)} + \frac{(x - x_0(t))\, \dot{\delta}(t)}{\delta^2(t)} \right).$$

Consequently, the Marangoni term simplifies to:

$$\beta \frac{h^2}{2}\nabla\Gamma = \frac{\beta\, h_0^2(t)\, \Gamma_0(t)\, H^2(\varsigma)}{2\, \delta(t)}\, \Phi'(\varsigma).$$

Furthermore, the pressure field is given by:

$$p = -\nabla \cdot (\nabla h - \beta\, \Gamma\, \nabla h)\,,$$

which in terms of similarity variables expands to:

$$\begin{aligned} p &= -\left(1-\beta\,\Gamma_0(t)\,\Phi(\varsigma)\right) h_0(t)\,H''(\varsigma)\frac{1}{\delta^2(t)} + \beta\,\Gamma_0(t)\,\Phi'(\varsigma)\,h_0(t)\,H'(\varsigma)\frac{1}{\delta^2(t)} \\ &= \frac{\beta\,h_0(t)\,\Gamma_0(t)\,(\Phi(\varsigma)\,H''(\varsigma)+\Phi'(\varsigma)\,H'(\varsigma)) - h_0(t)\,H''(\varsigma)}{\delta^2(t)}. \end{aligned}$$

We seek similarity solutions to the governing equations by proposing power-law scaling for each of the time-dependent amplitudes:

$$h_0(t) = t^a, \qquad \Gamma_0(t) = t^b, \qquad x_0(t) = t^c, \qquad \delta(t) = t^d.$$

For exact similarity solutions to exist, the exponents must balance across all terms in the evolution equations. We obtain the following set of exponents: $a = 1$, $b = 0$, $c = 1$, and $d = 1$.

These results are consistent with numerical observations. The scaling $x_0 \propto t$ agrees well with the numerical results shown in Figure 5.5c), where the neck displacement grows linearly in time. The exponent $b = 0$ suggests that Γ_0 remains constant, which is expected in the high-Pe regime where diffusion is absent. The assumption $h_0 \propto t$, however, is delicate. Numerically, the neck height appears nearly constant, but for the sake of analytical tractability, we proceed with $h_0 = vt$, where $v \ll u$, and u denotes the horizontal velocity scale.

With these assumptions, the similarity ansatz becomes:

$$h(x,t) = vt\,H(\varsigma), \qquad \Gamma(x,t) = \Gamma_0\,\Phi(\varsigma),$$

with the similarity variable defined as:

$$\varsigma = \frac{x-ut}{vt}.$$

Substituting these expressions into the height and surfactant transport equations, we arrive at the following coupled similarity ODE system:

$$\begin{aligned} -(v\varsigma+u)H' + vH + \left(\frac{H^3}{3}\left(H''-\beta\Gamma_0(\Phi H''+\Phi' H')\right)' - \frac{\beta\Gamma_0}{2}H^2\Phi'\right)' &= 0, \\ -(v\varsigma+u)\Gamma_0\Phi' + \left(-\beta\Gamma_0^2 H\Phi\Phi' - \frac{\Gamma_0}{2}H^2\Phi\left(H''-\beta\Gamma_0(\Phi H''+\Phi' H')\right)'\right)' &= 0. \end{aligned}$$

The validity and structure of this similarity system still require further investigation.

5.3.2 Traveling Wave Solutions

In the case of binary drops, Karpitschka and Riegler (2012) demonstrated both experimentally and theoretically that the balance between advective and diffusive volume fluxes in the neck region leads to a localized, temporarily stable surface tension gradient. This gradient induces a persistent Marangoni flow along the interface, which in turn stabilizes a traveling-wave-like configuration (Boatto et al., 1993), commonly referred to as the moving twin-drop state.

Assuming the neck moves at a constant speed v_n, the steady-state height equation (2.6) becomes:

$$-v_n \partial_x h + \nabla \cdot \left(-\frac{h^3}{3\mu} \nabla p - \frac{a h^2}{2\mu} \nabla \Gamma \right) = 0.$$

Integrating once with respect to x, we obtain:

$$-v_n h - \frac{h^3}{3\mu} \nabla p - \frac{a h^2}{2\mu} \nabla \Gamma = 0. \tag{5.1}$$

Meanwhile, for the surfactant field moving with a constant wave speed v_Γ, the traveling-wave solution of the transport equation takes the form:

$$-v_\Gamma \Gamma - \frac{1}{\mu} a h \Gamma \nabla \Gamma - \frac{1}{2\mu} h^2 \Gamma \nabla p = 0.$$

Solving for $\nabla \Gamma$, we get:

$$\nabla \Gamma = \frac{\mu}{a h} \left(-v_\Gamma - \frac{1}{2\mu} h^2 \nabla p \right). \tag{5.2}$$

Substituting (5.2) into (5.1), we arrive at a reduced form of the height evolution:

$$\left(-v_n + \frac{v_\Gamma}{2} \right) \partial_x h - \nabla \cdot \left(\frac{h^3}{12\mu} \nabla p \right) = 0.$$

This result resembles a modified version of Tanner's law for the classical spreading equation for a viscous drop. In future work, we aim to further investigate these traveling-wave solutions derived from this formulation.

5.4 Summary

In this chapter, we investigated the surprising transition from coalescence to non-coalescence behavior in the high-Péclet-number regime. Comparing low ($\beta = 0.1$) and high ($\beta = 0.5$) surfactant strengths at $Pe = 1000$ revealed distinct mechanisms. For $\beta > \beta_c$, monotonic surfactant profiles generate single-peaked Marangoni stress driving sustained neck motion. For $\beta < \beta_c$, bidirectional transport creates non-monotonic concentration profiles with opposing Marangoni peaks, inhibiting displacement.

Negative Marangoni stress generates interfacial vorticity, enabling escape from non-coalescence through boundary layer backflow. At very large Pe, kinematic shocks emerge with discontinuous velocity and concentration fields. The infinite-Pe limit admits interpretation through complex-variable formulations yielding Burgers-like equations. We derived similarity and traveling-wave frameworks for future analytical development.

6

CONCLUSION & OUTLOOK

This thesis has revealed how surfactants fundamentally alter the hydrodynamic singularity governing drop coalescence, transforming a classical problem in fluid mechanics into a rich landscape of new phenomena. Through systematic numerical simulations spanning three key dimensionless parameters – the surfactant strength number β, Péclet number Pe, and contact angle θ – we have uncovered a hierarchy of effects that emerge as surface chemistry couples to hydrodynamics. A central question motivating this work is how classical coalescence scalings are altered in the presence of surfactants. In particular, we seek to understand both vertical and horizontal bridge dynamics, especially since horizontal motion is absent in pure Newtonian coalescence.

In the diffusion-dominated regime ($Pe \ll 1$), surfactants primarily act to reduce the effective surface tension, preserving the self-similar character of coalescence while modifying its rate. The neck height evolution follows $h_0 = 0.272(1 - \beta\Gamma_0/2)\theta^4 t$, maintaining the classical linear-in-time scaling (Hernández-Sánchez et al., 2012) but with a surfactant-dependent prefactor. More remarkably, we discovered that Marangoni stresses break the symmetry of pure coalescence, driving horizontal neck motion with a universal $x_0 \propto t^{3/2}$ scaling – a phenomenon entirely absent in Newtonian systems. This horizontal displacement emerges from the interplay between surface tension gradients and the evolving bridge geometry, with our theoretical predictions matching simulations without any fitting parameters.

The transition to the advection-dominated regime ($Pe \gg 1$) reveals how surfactants can fundamentally restructure the coalescence singularity. Above a critical strength β_c, the system arrests into a stable non-coalescent state reminiscent of the twin-drop configurations observed experimentally (Karpitschka and Riegler, 2012). Below this threshold, we uncovered an unexpected mechanism: bidirectional surfactant transport creates non-monotonic concentration profiles that generate opposing Marangoni stresses. These stresses inject vorticity at the interface, enabling the system to escape non-coalescence through boundary layer backflow – a mechanism previously identified in filament pinch-off but not in coalescence dynamics.

At the extreme limit $Pe \to \infty$, entirely new singular phenomena emerge. Kinematic shocks form at the surfactant front, characterized by discontinuous velocity and pressure fields. Through a complex-variable reformulation, we demonstrated that these shocks satisfy a Burgers-like equation, connecting our results to the broader framework of nonlinear wave theory. This mathematical structure suggests that surfactant-laden interfaces can support shock solutions analogous to those in compressible flow, despite operating in the Stokes regime.

6.1 Broader Implications

Our findings have both fundamental and practical implications. From a fundamental perspective, this work demonstrates that surfactants do not merely modify existing hydrodynamic singularities – they can generate qualitatively new singular behavior. The emergence of shock discontinuities in Stokes flow challenges conventional understanding of low-Reynolds-number hydrodynamics, where such phenomena are typically absent. The vorticity generation mechanism we identified provides a unifying framework for understanding escape from singular states across different interfacial flow problems (Kamat et al., 2020; Constante-Amores et al., 2021).

Our results provide predictive tools for controlling coalescence in industrial processes. The phase diagram delineating coalescence, non-coalescence, and arrested states establishes design principles for applications from inkjet printing to emulsion stability. The critical surfactant strength β_c serves as a design threshold: systems below this value will eventually coalesce regardless of Péclet number, while those above achieve persistent non-coalescence. The temporal boundary layer concept provides a framework for predicting Marangoni-dominated regimes, analogous to the Grossmann-Lohse theory for thermally driven turbulence (Grossmann and Lohse, 2000; Grossmann and Lohse, 2001; Lohse and Shishkina, 2023; Lohse and Shishkina, 2024) and the Sanjay-Lohse theory for impacting drops (Sanjay and Lohse, 2025). Adapting this temporal boundary layer framework could enable predictions crucial for rapid droplet interaction processes.

The horizontal displacement scaling $x_f \sim \beta Pe$ in the low-Pe regime suggests strategies for controlling droplet positioning through surfactant design. In pharmaceutical or food emulsions where precise droplet placement matters, this relationship enables quantitative prediction of Marangoni-driven motion. Conversely, the non-monotonic behavior at high Pe warns that simply increasing surfactant transport rates may not enhance displacement, important for optimization of industrial mixing processes.

6.2 Limitations and Open Questions

While our lubrication-based approach captures the essential physics for small contact angles ($\theta \lesssim 45°$), extending to larger angles requires full Stokes flow simulations. The computational challenges are substantial: resolving thin precursor films while maintaining numerical stability at high angles remains an open problem. Our two-dimensional approximation, while revealing the fundamental scalings, neglects three-dimensional effects that may become important for transverse instabilities or asymmetric surfactant distributions.

Several intriguing questions emerge from our analysis. Why does the negative Marangoni stress peak intensify monotonically with Pe for $\beta < \beta_c$? Is there a universal mechanism governing this enhancement, perhaps related to the shock formation process? The connection between our complex-variable formulation and the full three-dimensional problem remains unexplored—do similar mathematical structures exist beyond the lubrication limit?

The role of surfactant solubility, deliberately excluded here by considering only insoluble surfactants, presents another frontier. Soluble surfactants introduce bulk-surface exchange, potentially stabilizing or destabilizing the phenomena we observed. The interplay between Marangoni stresses and sorption kinetics could yield new dynamical regimes, particularly near the critical strength β_c.

6.3 Future Directions

Several concrete research directions emerge from this work:

- **Theoretical Extensions**: The similarity and traveling-wave frameworks introduced in Chapter 5 require further development. Completing the analysis of the similarity ODEs could reveal whether true self-similar solutions exist in the high-Pe limit (Eggers and Fontelos, 2015). The traveling-wave formulation, connecting to modified Tanner's law, may yield analytical solutions for the non-coalescent state that could be compared with experiments (Giacomelli et al., 2016).
- **Three-Dimensional Dynamics**: Extending our model to capture azimuthal variations and transverse bridge dynamics (width w_0) would enable study of instabilities absent in two dimensions (Diddens and Rocha, 2024). This is particularly relevant for understanding whether the vorticity generation mechanism we identified can trigger three-dimensional flow structures.
- **Beyond Lubrication**: Developing efficient numerical methods for full Stokes flow with surfactant transport would enable exploration of high-angle coalescence approaching the jumping regime ($\theta \to 90^\circ$) (Wasserfall et al., 2017). This could reveal whether shock formation persists beyond the lubrication limit and how Marangoni stresses compete with inertial effects.
- **Experimental Validation**: Our predictions for horizontal displacement scaling and the critical transition at β_c are directly testable. High-speed imaging combined with controlled surfactant addition could verify the $t^{3/2}$ scaling and map the phase boundaries we predict. The shock phenomena at high Pe may be observable using appropriate visualization techniques.
- **Complex Surfactant Systems**: Real surfactants often exhibit non-linear isotherms,

cooperative effects, and phase transitions (Manikantan and Squires, 2020; Anthony et al., 2023). Incorporating these complexities could reveal new phenomena, particularly near the coalescence/non-coalescence boundary where small changes in surface behavior may have dramatic effects.

6.4 Closing Perspective

This thesis demonstrates that even classical fluid mechanics problems can harbor surprising complexity when surface chemistry enters the picture. The coupling between surfactant transport and hydrodynamics transforms drop coalescence from a well-understood capillary-driven process into a rich dynamical system exhibiting shocks, vorticity generation, and arrested states. As we push toward smaller scales in technology – from microfluidics to targeted drug delivery – understanding these surfactant-mediated phenomena becomes not just scientifically fascinating but technologically essential. The framework developed here, combining high-fidelity simulation with theoretical analysis, provides a foundation for controlling coalescence across the spectrum from violent merger to delicate non-coalescence, opening new possibilities for manipulating fluid interfaces at the microscale.

7

Code Listings

Scan the QR code for code access

BIBLIOGRAPHY

Aarts, Dirk GAL et al. (2005). "Hydrodynamics of droplet coalescence". In: *Physical review letters* 95.16, p. 164503.

Anderson, John D (2005). "Ludwig Prandtl's boundary layer". In: *Physics today* 58.12, pp. 42–48.

Anthony, Christopher R et al. (2023). "Sharp interface methods for simulation and analysis of free surface flows with singularities: Breakup and coalescence". In: *Annual Review of Fluid Mechanics* 55.1, pp. 707–747.

Ashgriz, N. (2011). *Handbook of atomization and sprays: theory and applications*. Springer Science & Business Media.

Ashgriz, N. and J. Y. Poo (1990). "Coalescence and separation in binary collisions of liquid drops". In: *Journal of Fluid Mechanics* 221, pp. 183–204.

Basaran, Osman A., Haijing Gao, and Pradeep P. Bhat (Jan. 2013). "Nonstandard Inkjets". In: *Annual Review of Fluid Mechanics* 45.1, pp. 85–113. ISSN: 1545-4479.

Berg, Steffen (2009). "Marangoni-driven spreading along liquid-liquid interfaces". In: *Physics of Fluids* 21.3.

Boatto, Stefanella, Leo P Kadanoff, and Piero Olla (1993). "Traveling-wave solutions to thin-film equations". In: *Physical Review E* 48.6, p. 4423.

Boerhaave, H. (1732). *Elementa Chemiae*. Vol. 1. Lugduni Batavorum. Leiden.

Bruning, Myrthe A et al. (2018). "Delayed coalescence of surfactant containing sessile droplets". In: *Physical review fluids* 3.7, p. 073605.

Caragine, C. M., S. C. Haley, and A. Zidovska (2018). "Surface fluctuations and coalescence of nucleolar droplets in the human cell nucleus". In: *Physical Review Letters* 121, p. 148101.

Ceniceros, Hector D (2003). "The effects of surfactants on the formation and evolution of capillary waves". In: *Physics of Fluids* 15.1, pp. 245–256.

Champougny, Lorène et al. (Dec. 2024). "Interfacial Dripping Faucet: Generating Monodisperse Liquid Lenses". In: *Physical Review Letters* 133.25. ISSN: 1079-7114.

Chesters, AK (1991). "The modelling of coalescence processes in fluid-liquid dispersions: a review of current understanding". In: *Chemical Engineering Research and Design* 69, pp. 259–270.

Childress, Stephen and Jerome K Percus (1981). "Nonlinear aspects of chemotaxis". In: *Mathematical Biosciences* 56.3-4, pp. 217–237.

Christian Bauer, Alexander Frink and Richard Kreckel (2002). “Introduction to the GiNaC Framework for Symbolic Computation within the C++ Programming Language”. In: *J. Symb. Comput.* 33.1, pp. 1–12. ISSN: 0747-7171. DOI: `https://doi.org/10.1006/jsco.2001.0494`.

Constante-Amores, CR et al. (2021). “Role of surfactant-induced Marangoni stresses in drop-interface coalescence”. In: *Journal of Fluid Mechanics* 925, A15.

Crank, John (1979). *The mathematics of diffusion*. Oxford university press.

Craster, Richard V and Omar K Matar (2009). “Dynamics and stability of thin liquid films”. In: *Reviews of Modern Physics* 81.3, pp. 1131–1198.

Crowdy, Darren G (2021). “Viscous Marangoni flow driven by insoluble surfactant and the complex Burgers equation”. In: *SIAM Journal on Applied Mathematics* 81.6, pp. 2526–2546.

Da Vinci, Leonardo (1508). *The notebooks of Leonardo da Vinci*. George Braziller, New York.

Da Vinci, Leonardo (1980). *Codex Leicester*. Christie’s, London.

Daly, Ronan et al. (Oct. 2015). “Inkjet printing for pharmaceutics – A review of research and manufacturing”. In: *International Journal of Pharmaceutics* 494.2, pp. 554–567. ISSN: 0378-5173.

Davis, R. H., J. A. Schonberg, and J. M. Rallison (1989). “The lubrication force between two viscous drops”. In: *Physics of Fluids A: Fluid Dynamics* 1.1, pp. 77–81.

Day, Richard F, E John Hinch, and John R Lister (1998). “Self-similar capillary pinchoff of an inviscid fluid”. In: *Physical review letters* 80.4, p. 704.

de Gennes, P.-G., F. Brochard-Wyart, and D. Quéré (2003). *Capillarity and wetting phenomena: drops, bubbles, pearls, waves*. Springer Science & Business Media.

Diddens, Christian and Duarte Rocha (2024). “Bifurcation tracking on moving meshes and with consideration of azimuthal symmetry breaking instabilities”. In: *J. Comput. Phys.* 518, p. 113306. ISSN: 0021-9991. DOI: `https://doi.org/10.1016/j.jcp.2024.113306`.

Dixit, Ayush et al. (2025). “Viscoelastic Worthington jets and droplets produced by bursting bubbles”. In: *Journal of Fluid Mechanics* 1010, A2.

Eggers, Jens (1993). “Universal pinching of 3D axisymmetric free-surface flow”. In: *Physical review letters* 71.21, p. 3458.

Eggers, Jens (July 1997). “Nonlinear dynamics and breakup of free-surface flows”. In: *Reviews of Modern Physics* 69.3, pp. 865–930. ISSN: 1539-0756.

Eggers, Jens and Marco Fontelos (2015). *Singularities: formation, structure, and propagation*. Vol. 53. Cambridge University Press.

Eggers, Jens and Marco A Fontelos (2008). “The role of self-similarity in singularities of partial differential equations”. In: *Nonlinearity* 22.1, R1.

Eggers, Jens, John R Lister, and Howard A Stone (1999). “Coalescence of liquid drops”. In: *Journal of Fluid Mechanics* 401, pp. 293–310.

Eggers, Jens, James E Sprittles, and Jacco H Snoeijer (2024). “Coalescence dynamics”. In: *Annual Review of Fluid Mechanics* 57.

Eshima, Jun, Luc Deike, and Howard A Stone (2024). “Thin-film flow due to an asymmetric distribution of surface tension and applications to surfactant deposition”. In: *Journal of Fluid Mechanics* 992, A2.

Gaver, Donald P and James B Grotberg (1990). “The dynamics of a localized surfactant on a thin film”. In: *Journal of Fluid Mechanics* 213, pp. 127–148.

Giacomelli, Lorenzo, Manuel V Gnann, and Felix Otto (2016). “Rigorous asymptotics of traveling-wave solutions to the thin-film equation and Tanner’s law”. In: *Nonlinearity* 29.9, p. 2497.

Grossmann, S. and D. Lohse (2000). “Scaling in thermal convection: a unifying theory”. In: *J. Fluid Mech.* 407, pp. 27–56. DOI: `10.1017/S0022112099007545`.

Grossmann, S. and D. Lohse (2001). “Thermal convection for large Prandtl numbers”. In: *Phys. Rev. Lett.* 86.15, p. 3316. DOI: `10.1103/PhysRevLett.86.3316`.

Heil, Matthias and Andrew L Hazel (2006). “oomph-lib–An Object-Oriented Multi-Physics Finite-Element Library”. In: *Fluid-structure interaction: Modelling, simulation, optimisation*. Springer, pp. 19–49.

Hernández-Sánchez, JF et al. (2012). “Symmetric and asymmetric coalescence of drops on a substrate”. In: *Physical review letters* 109.18, p. 184502.

Hoepffner, Jérôme and Gounséti Paré (2013). “Recoil of a liquid filament: escape from pinch-off through creation of a vortex ring”. In: *Journal of fluid mechanics* 734, pp. 183–197.

Hofsäss, Hans and Kun Zhang (2008). “Surfactant sputtering”. In: *Applied Physics A* 92, pp. 517–524.

Hosoi, A. E. and J. W. M. Bush (2001). “Evaporative instabilities in climbing films”. In: *J. Fluid Mech.* 442, pp. 217–239.

Jaworek, A. and A.T. Sobczyk (Mar. 2008). “Electrospraying route to nanotechnology: An overview”. In: *Journal of Electrostatics* 66.3–4, pp. 197–219. ISSN: 0304-3886.

Kamat, Pritish M et al. (2020). “Surfactant-driven escape from endpinching during contraction of nearly inviscid filaments”. In: *Journal of Fluid Mechanics* 899, A28.

Kaneelil, Paul R et al. (2022). “Three-dimensional self-similarity of coalescing viscous drops in the thin-film regime”. In: *Physical review letters* 129.14, p. 144501.

Karpitschka, Stefan and Hans Riegler (2012). “Noncoalescence of Sessile Drops from Different but Miscible Liquids: Hydrodynamic Analysis of the Twin Drop Contour as a Self-Stabilizing Traveling Wave”. In: *Physical Review Letters* 109.6, p. 066103.

Karpitschka, Stefan and Hans Riegler (2014). “Sharp transition between coalescence and non-coalescence of sessile drops”. In: *Journal of Fluid Mechanics* 743, R1.

Kavehpour, H. Pirouz (2015). “Coalescence of drops”. In: *Annual Review of Fluid Mechanics* 47, pp. 245–268.

Keller, Joseph B (1983). “Breaking of liquid films and threads”. In: *Physics of Fluids* 26.12, pp. 3451–3453.

Kim, S. et al. (2020). “How a raindrop gets shattered on biological surfaces”. In: *Proc. Natl. Acad. Sci.* 117.25, pp. 13901–13907.

Kistler, S. F. and L. E. Scriven (Mar. 1984). "Coating flow theory by finite element and asymptotic analysis of the navier-stokes system". In: *International Journal for Numerical Methods in Fluids* 4.3, pp. 207–229. ISSN: 1097-0363.

Kresheck, Gordon C (1975). "Surfactants". In: *Water A Comprehensive Treatise: Aqueous Solutions of Amphiphiles and Macromolecules*. Springer, pp. 95–167.

Lefebvre, Arthur (Dec. 1988). *Atomization and Sprays*. CRC Press. ISBN: 9781482227857.

Leidenfrost, J. G. (1756). *De aquae communis nonnullis qualitatibus tractatus*. Ovenius.

Liao, Y. and D. Lucas (2010). "A literature review on mechanisms and models for the coalescence process of fluid particles". In: *Chemical Engineering Science* 65.10, pp. 2851–2864.

Lohse, D. and O. Shishkina (2023). "Ultimate turbulent thermal convection". In: *Phys. Today* 76.11, pp. 26–32. DOI: `10.1063/PT.3.5341`.

Lohse, D. and O. Shishkina (2024). "Ultimate Rayleigh–Bénard turbulence". In: *Rev. Mod. Phys.* 96, p. 035001.

Lohse, D. and E. Villermaux (2020). "Double threshold behavior for breakup of liquid sheets". In: *Proc. Natl. Acad. Sci.* 117.32, pp. 18912–18914.

Lohse, Detlef (Jan. 2022). "Fundamental Fluid Dynamics Challenges in Inkjet Printing". In: *Annual Review of Fluid Mechanics* 54.1, pp. 349–382. ISSN: 1545-4479.

Lord Rayleigh (1878). "The influence of electricity on colliding water drops". In: *Proc. R. Soc. Lond.*, pp. 405–409.

Lundgren, Thomas and Petros Koumoutsakos (1999). "On the generation of vorticity at a free surface". In: *Journal of Fluid Mechanics* 382, pp. 351–366.

Manikantan, Harishankar and Todd M Squires (2020). "Surfactant dynamics: hidden variables controlling fluid flows". In: *Journal of fluid mechanics* 892, P1.

Mariotte, Edme (1686). *Traité du mouvement des caux et des autres corps fluides*. E Michallet, Paris.

McKinley, Gareth H (2005). "Dimensionless groups for understanding free surface flows of complex fluids". In.

Munro, James P et al. (2015). "Thin-sheet flow between coalescing bubbles". In: *Journal of Fluid Mechanics* 773, R3.

Oron, Alexander, Stephen H Davis, and S George Bankoff (1997). "Long-scale evolution of thin liquid films". In: *Reviews of modern physics* 69.3, p. 931.

Passot, T et al. (1995). "Instability of strained vortex layers and vortex tube formation in homogeneous turbulence". In: *Journal of Fluid Mechanics* 282, pp. 313–338.

Paulsen, J. D. (2013). "Approach and coalescence of liquid drops in air". In: *Physical Review E* 88.6, p. 063010.

Plateau, J. (July 1857). "I. Experimental and theoretical researches on the figures of equilibrium of a liquid mass withdrawn from the action of gravity.–Third series". In: *The London, Edinburgh, and Dublin Philosophical Magazine and Journal of Science* 14.90, pp. 1–22. ISSN: 1941-5990.

Pokluda, O., C. T. Bellehumeur, and J. Vlachopoulos (1997). "Modification of Frenkel's model for sintering". In: *AIChE Journal* 43.12, pp. 3253–3256.

Ptasinski, K. J. and P. J. A. M. Kerkhof (July 1992). "Electric Field Driven Separations: Phenomena and Applications". In: *Separation Science and Technology* 27.8–9, pp. 995–1021. ISSN: 1520-5754.

Quéré, D. (2013). "Leidenfrost dynamics". In: *Annu. Rev. Fluid Mech.* 45.1, pp. 197–215.

Rayleigh, Lord (1879). "On the capillary phenomena of jets". In: *Proceedings of the Royal Society of London*, pp. 71–97.

Rayleigh, Lord (1892). "XVI. On the instability of a cylinder of viscous liquid under capillary force". In: *The London, Edinburgh, and Dublin Philosophical Magazine and Journal of Science* 34.207, pp. 145–154.

Rood, Edwin P (1994). "Interpreting vortex interactions with a free surface". In: *Journal of Fluids Engineering*.

Saffman, PG and M Delbrück (1975). "Brownian motion in biological membranes." In: *Proceedings of the National Academy of Sciences* 72.8, pp. 3111–3113.

Sanjay, Vatsal and Detlef Lohse (2025). "Unifying theory of scaling in drop impact: Forces & maximum spreading diameter". In: *Phys. Rev. Lett.* 134, p. 104003. DOI: `10.1103/PhysRevLett.134.104003`.

Sauleda, Madeline L et al. (2022). "Surfactant spreading on a deep subphase: Coupling of Marangoni flow and capillary waves". In: *Journal of colloid and interface science* 614, pp. 511–521.

Savart, Félix (1833). "Mémoire sur la constitution des veines liquids lancees par des orifices circulaires en mince paroi". In: *Ann. de Chim.* 53, pp. 337–386.

Shen, Amy Q et al. (2002). "Fiber coating with surfactant solutions". In: *Physics of Fluids* 14.11, pp. 4055–4068.

Snoeijer, Jacco H. and Bruno Andreotti (Jan. 2013). "Moving Contact Lines: Scales, Regimes, and Dynamical Transitions". In: *Annual Review of Fluid Mechanics* 45.1, pp. 269–292. ISSN: 1545-4479.

Sornette, Didier and Anders Johansen (1997). "Large financial crashes". In: *Physica A: Statistical Mechanics and its Applications* 245.3-4, pp. 411–422.

Sprittles, J. E. (2024). "Gas microfilms in droplet dynamics: When do drops bounce?" In: *Annual Review of Fluid Mechanics* 56, pp. 67–89.

Tao, Terence (2019). "Searching for singularities in the Navier–Stokes equations". In: *Nature Reviews Physics* 1.7, pp. 418–419.

Taylor, G. I. (1964). "Disintegration of water drops in an electric field". In: *Proc. R. Soc. Lond. A* 280.1382, pp. 383–397.

Temprano-Coleto, Fernando and Howard A Stone (2024). "On the self-similarity of unbounded viscous Marangoni flows". In: *Journal of Fluid Mechanics* 997, A45.

Thess, A, D Spirn, and B Jüttner (1995). "Viscous flow at infinite Marangoni number". In: *Physical Review Letters* 75.25, p. 4614.

Thiele, Uwe, Andrew J Archer, and Mathis Plapp (2012). "Thermodynamically consistent description of the hydrodynamics of free surfaces covered by insoluble surfactants of high concentration". In: *Physics of Fluids* 24.10.

Thomson, Joseph John and Hugh Frank Newall (1886). "V. On the formation of vortex rings by drops falling into liquids, and some allied phenomena". In: *Proceedings of the Royal Society of London* 39.239-241, pp. 417–436.

Verdier, C. (2001). "The influence of the viscosity ratio on polymer droplet collision in quiescent blends". In: *Polymer* 42.16, pp. 6999–7007.

Villermaux, Emmanuel and Benjamin Bossa (July 2009). "Single-drop fragmentation determines size distribution of raindrops". In: *Nature Physics* 5.9, pp. 697–702. ISSN: 1745-2481.

Volonteri, Marta, Mélanie Habouzit, and Monica Colpi (2021). "The origins of massive black holes". In: *Nature Reviews Physics* 3.11, pp. 732–743.

Wasserfall, Joram et al. (2017). "Coalescence-induced droplet jumping on superhydrophobic surfaces: Effects of droplet mismatch". In: *Physical Review Fluids* 2.12, p. 123601.

Whitham, Gerald Beresford (1974). *Linear and nonlinear waves*. John Wiley & Sons.

Zhang, Wendy W and John R Lister (1999). "Similarity solutions for van der Waals rupture of a thin film on a solid substrate". In: *Physics of Fluids* 11.9, pp. 2454–2462.

Appendices

A

DERIVATION OF LUBRICATION EQUATIONS FOR THIN LIQUID FILMS

We study a thin film of Newtonian liquid with an initial thickness profile given by $h(x, y)$. We use a Cartesian coordinate system (x, y, z), placing the origin at the solid-liquid interface at the center of the film. The free surface of the liquid is described by the height function $z = h(x, y, t)$. At this surface, the *unit normal vector* $\mathbf{n}$ and the *tangent vector* $\mathbf{t}$ can be defined. The normal vector is given by:

$$\mathbf{n} = \frac{1}{N}\left(-\frac{\partial h}{\partial x}, -\frac{\partial h}{\partial y}, 1\right), \quad \text{with} \quad N = \sqrt{1 + \left(\frac{\partial h}{\partial x}\right)^2 + \left(\frac{\partial h}{\partial y}\right)^2}$$

The evolution of the liquid film is governed by the incompressible Navier–Stokes equations, which describe the conservation of momentum:

$$\rho\left(\frac{\partial \mathbf{u}}{\partial t} + \mathbf{u}\cdot\nabla\mathbf{u}\right) = -\nabla p + \mu\nabla^2\mathbf{u}, \tag{A.1}$$

and the continuity equation for an incompressible fluid, ensuring mass conservation:

$$\nabla\cdot\mathbf{u} = 0. \tag{A.2}$$

Here, $\mathbf{u} = (u_x, u_y, u_z)$ denotes the velocity field, p is the pressure, while ρ and μ represent the fluid density and dynamic viscosity, respectively.

We use the following scaled variables:

$$\bar{x} \equiv \frac{x}{L}, \quad \bar{y} \equiv \frac{y}{L}, \quad \bar{z} \equiv \frac{z}{H}, \quad \bar{u}_x \equiv \frac{u_x}{U_0}, \quad \bar{u}_y \equiv \frac{u_y}{U_0},$$

$$\bar{u}_z \equiv \frac{u_z}{W_0}, \quad \bar{t} \equiv \frac{U_0 t}{L}, \quad \bar{p} \equiv \frac{H^2 p}{\mu U_0 L}.$$

In this work, we consider systems with thin liquid films, for which the aspect ratio $\varepsilon = \frac{H}{L} \ll 1$ is small.

After introducing the scaled variables, the continuity equation becomes:

$$0 = \nabla \cdot \mathbf{u} = \frac{U_0}{L}\frac{\partial \bar{u}_x}{\partial \bar{x}} + \frac{U_0}{L}\frac{\partial \bar{u}_y}{\partial \bar{y}} + \frac{W_0}{H}\frac{\partial \bar{u}_z}{\partial \bar{z}} \Rightarrow \frac{\partial \bar{u}_x}{\partial \bar{x}} + \frac{\partial \bar{u}_y}{\partial \bar{y}} + \frac{W_0 L}{U_0 H}\frac{\partial \bar{u}_z}{\partial \bar{z}} = 0.$$

Assuming that all terms in the continuity equation are of comparable magnitude leads to the scaling

$$W_0 = \varepsilon U_0$$

for the vertical velocity component.

The scaled x-component of the Navier–Stokes equation then reads:

$$\rho\left(\frac{U_0^2}{L}\frac{\partial \bar{u}_x}{\partial \bar{t}} + \frac{U_0^2}{L}\bar{u}_x\frac{\partial \bar{u}_x}{\partial \bar{x}} + \frac{U_0^2}{L}\bar{u}_y\frac{\partial \bar{u}_x}{\partial \bar{y}} + \frac{\varepsilon U_0^2}{H}\bar{u}_z\frac{\partial \bar{u}_x}{\partial \bar{z}}\right) - \frac{\mu}{L}\frac{\partial \bar{p}}{\partial \bar{x}} + \mu\left(\frac{U_0}{L^2}\frac{\partial^2 \bar{u}_x}{\partial \bar{x}^2} + \frac{U_0}{L^2}\frac{\partial^2 \bar{u}_x}{\partial \bar{y}^2} + \frac{U_0}{H^2}\frac{\partial^2 \bar{u}_x}{\partial \bar{z}^2}\right) = 0.$$

$$\frac{\rho U_0 H}{\mu}\frac{H}{L}\left(\frac{\partial \bar{u}_x}{\partial \bar{t}} + \bar{u}_x\frac{\partial \bar{u}_x}{\partial \bar{x}} + \bar{u}_y\frac{\partial \bar{u}_x}{\partial \bar{y}} + \bar{u}_z\frac{\partial \bar{u}_x}{\partial \bar{z}}\right) = -\frac{\partial \bar{p}}{\partial \bar{x}} + \frac{\partial^2 \bar{u}_x}{\partial \bar{z}^2} + \varepsilon^2\left(\frac{\partial^2 \bar{u}_x}{\partial \bar{x}^2} + \frac{\partial^2 \bar{u}_x}{\partial \bar{y}^2}\right)$$

Assuming that $Re \ll 1$ and $\varepsilon^2 \ll 1$, we obtain the leading-order approximation of the scaled x-momentum equation:

$$-\frac{\partial \bar{p}}{\partial \bar{x}} + \frac{\partial^2 \bar{u}_x}{\partial \bar{z}^2} = 0.$$

In a similar manner, the other components of the Navier–Stokes equations reduce to the following dimensional forms:

$$\begin{aligned} -\frac{\partial p}{\partial x} + \mu\frac{\partial^2 u_x}{\partial z^2} &= 0, \\ -\frac{\partial p}{\partial y} + \mu\frac{\partial^2 u_y}{\partial z^2} &= 0, \\ -\frac{\partial p}{\partial z} &= 0. \end{aligned}$$

The last equation implies that the pressure $p = p(x, y)$ is independent of the vertical coordinate z.

At the solid–liquid interface $z = 0$, we apply no-slip boundary conditions:

$$u_x(z = 0) = 0, \quad u_y(z = 0) = 0.$$

At the free surface $z = h(x, y, t)$, the normal and tangential stress balances are given by:

$$p - p_a - \tau_{nn} + 2H\gamma = 0,$$

$$\tau_{nt} + \mathbf{t} \cdot \nabla_s \gamma = 0,$$

where γ is the surface tension, H is the mean curvature, τ_{nn} and τ_{nt} are the normal and tangential stress components, and $\mathbf{t}$ is the tangential unit vector along the interface. Assuming that the viscous normal stresses are negligible at a liquid-air interface yields

$$p - p_a = -\gamma \nabla_s \cdot \mathbf{n}$$

The surface gradient operator ∇_s applies to any function defined on the free surface $z = h(x, y)$, and is given by:

$$\nabla_s = (\mathbb{I} - \mathbf{nn})\nabla,$$

where $\mathbf{n}$ is the unit normal vector to the surface, and $\mathbb{I}$ is the identity matrix.

In Cartesian coordinates, this operator expands to:

$$\frac{1}{N^2}\left(\left[1+\left(\frac{\partial h}{\partial y}\right)^2\right]\frac{\partial}{\partial x} - \frac{\partial h}{\partial x}\frac{\partial h}{\partial y}\frac{\partial}{\partial y} + \left[1+\left(\frac{\partial h}{\partial x}\right)^2\right]\frac{\partial}{\partial y}\right),$$

where $N = \sqrt{1 + \left(\frac{\partial h}{\partial x}\right)^2 + \left(\frac{\partial h}{\partial y}\right)^2}$.

The mean curvature of the interface is then expressed as:

$$\nabla_s \cdot \mathbf{n} = \frac{\left[1+\left(\frac{\partial h}{\partial y}\right)^2\right]\frac{\partial^2 h}{\partial x^2} + \left[1+\left(\frac{\partial h}{\partial x}\right)^2\right]\frac{\partial^2 h}{\partial y^2} - 2\frac{\partial h}{\partial x}\frac{\partial h}{\partial y}\frac{\partial^2 h}{\partial x \partial y}}{\left(1+\left(\frac{\partial h}{\partial x}\right)^2 + \left(\frac{\partial h}{\partial y}\right)^2\right)^{3/2}}.$$

After applying the scaling and neglecting terms of order ε, the mean curvature simplifies to:

$$\nabla_s \cdot \mathbf{n} = \frac{\partial^2 h}{\partial x^2} + \frac{\partial^2 h}{\partial y^2}.$$

Hence, the capillary pressure becomes:

$$p = -\gamma\left(\frac{\partial^2 h}{\partial x^2} + \frac{\partial^2 h}{\partial y^2}\right).$$

Assuming negligible viscous stresses in the gas phase, the tangential stress balance at the interface $z = h(x, y, t)$ yields:

$$\mu \left.\frac{\partial u_x}{\partial z}\right|_{z=h} = \frac{\partial \gamma}{\partial x}, \qquad \mu \left.\frac{\partial u_y}{\partial z}\right|_{z=h} = \frac{\partial \gamma}{\partial y}.$$

The liquid-air interface is defined by the scalar function $f(x, y, z, t) = z - h(x, y, t) = 0$. For a non-volatile liquid, this interface is a material surface, which implies:

$$\frac{Df}{Dt} = \frac{\partial f}{\partial t} + \mathbf{u} \cdot \nabla f = 0,$$

or equivalently,

$$-\frac{\partial h}{\partial t} - \frac{\partial h}{\partial x} u_x\Big|_{z=h(x,y,t)} - \frac{\partial h}{\partial y} u_y\Big|_{z=h(x,y,t)} + u_z\Big|_{z=h(x,y,t)} = 0.$$

Next, we integrate the incompressibility condition with respect to z from 0 to h:

$$\int_0^h \left(\frac{\partial u_x}{\partial x} + \frac{\partial u_y}{\partial y}\right) dz + u_z\Big|_{z=h} - u_z\Big|_{z=0} = 0.$$

Using the Leibniz rule and noting that $u_z(z = 0) = 0$ due to the no-penetration boundary condition at the substrate, this becomes:

$$-u_z\Big|_{z=h(x,y,t)} = \frac{\partial}{\partial x} \int_0^h u_x \, dz - \frac{\partial h}{\partial x} u_x\Big|_{z=h} + \frac{\partial}{\partial y} \int_0^h u_y \, dz - \frac{\partial h}{\partial y} u_y\Big|_{z=h}.$$

Substituting this into the earlier kinematic condition yields the evolution equation for the height:

$$\frac{\partial h}{\partial t} + \frac{\partial}{\partial x} \int_0^h u_x \, dz + \frac{\partial}{\partial y} \int_0^h u_y \, dz = 0.$$

We integrate the Navier–Stokes equations using the boundary conditions specified earlier, noting that the pressure p and its gradients $\frac{\partial p}{\partial x}$ and $\frac{\partial p}{\partial y}$ are independent of z. The resulting expressions for the velocity components are:

$$u_x(x, y, z) = \frac{1}{\mu}\frac{\partial p}{\partial x}\left(\frac{z^2}{2} - hz\right) + \frac{1}{\mu}\frac{\partial \gamma}{\partial x} z,$$

$$u_y(x, y, z) = \frac{1}{\mu}\frac{\partial p}{\partial y}\left(\frac{z^2}{2} - hz\right) + \frac{1}{\mu}\frac{\partial \gamma}{\partial y} z.$$

Substituting these velocity profiles into the height evolution equation yields the lubrication equation:

$$\frac{\partial h}{\partial t} + \nabla \cdot \left[\frac{1}{2\mu} h^2 \nabla\gamma - \frac{1}{3\mu} h^3 \nabla p\right] = 0.$$

$$p = -\nabla(\gamma \nabla h).$$

B

SURFACTANT ADVECTION DIFFUSION EQUATION AT THE INTERFACE

The transport of surfactants along the free surface $z = h(x, y, t)$ is described by the surface convection-diffusion equation:

$$\frac{\partial \Gamma}{\partial t} + \nabla_s \cdot \left(\Gamma \, \mathbf{u} \big|_{z=h(x,y)} \right) = J + D_s \nabla_s^2 \Gamma,$$

where Γ is the surfactant concentration on the interface, D_s is the surface diffusivity, and J is the flux between the interface and the bulk. For an insoluble surfactant, this flux vanishes, i.e., $J = 0$.

Using the definition of the surface gradient operator and neglecting higher-order terms in ε, the surface divergence term simplifies to:

$$\nabla_s \cdot (\Gamma \mathbf{u}) \approx \frac{\partial}{\partial x} \left(\Gamma \, u_x(x, y, z = h) \right) + \frac{\partial}{\partial y} \left(\Gamma \, u_y(x, y, z = h) \right).$$

Evaluating the velocity expressions at the free surface yields:

$$u_x(x, y, z = h) = \frac{1}{\mu} \frac{\partial p}{\partial x} \left(-\frac{h^2}{2} \right) + \frac{1}{\mu} \frac{\partial \gamma}{\partial x} h,$$

$$u_y(x, y, z = h) = \frac{1}{\mu} \frac{\partial p}{\partial y} \left(-\frac{h^2}{2} \right) + \frac{1}{\mu} \frac{\partial \gamma}{\partial y} h.$$

Substituting these expressions into the surfactant transport equation leads to the final form of the convection-diffusion equation at the interface:

$$\frac{\partial \Gamma}{\partial t} + \nabla \cdot \left[\frac{1}{\mu} h \Gamma \nabla \gamma - \frac{1}{2\mu} h^2 \Gamma \nabla p - D_s \nabla \Gamma \right] = J,$$

where the operator $\nabla \equiv \left(\frac{\partial}{\partial x}, \frac{\partial}{\partial y} \right)$ denotes the two-dimensional gradient.